"Hybrid" plasma spraying of NiCrAlY + Al_2O_3 + h-BN composite coatings for sliding wear applications

Giovanni Bolelli, Alessia Candeli, Luca Lusvarghi, Tiziano Manfredini, Alain Denoirjean, Stéphane Valette, Alice Ravaux, Erick Meillot

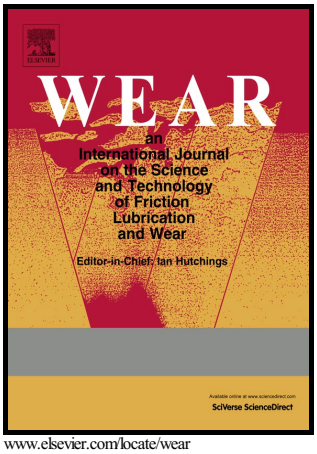

www.elsevier.com/locate/wear

PII: S0043-1648(16)30353-2
DOI: http://dx.doi.org/10.1016/j.wear.2017.02.027
Reference: WEA102081

To appear in: *Wear*

Received date: 22 September 2016
Revised date: 29 January 2017
Accepted date: 10 February 2017

Cite this article as: Giovanni Bolelli, Alessia Candeli, Luca Lusvarghi, Tiziano Manfredini, Alain Denoirjean, Stéphane Valette, Alice Ravaux and Erick Meillot, "Hybrid" plasma spraying of NiCrAlY + Al_2O_3 + h-BN composite coatings for sliding wear applications, *Wear,* http://dx.doi.org/10.1016/j.wear.2017.02.027

"Hybrid" plasma spraying of NiCrAlY + Al_2O_3 + *h*-BN composite coatings for sliding wear applications

Giovanni Bolelli[1*], Alessia Candeli[1], Luca Lusvarghi[1,2], Tiziano Manfredini[1,2], Alain Denoirjean[3], Stéphane Valette[3], Alice Ravaux[3], Erick Meillot[4]

[1]Department of Engineering "Enzo Ferrari", University of Modena and Reggio Emilia, Via P. Vivarelli 10/1, 41125 Modena (MO), Italy

[2]Consorzio Interuniversitario Nazionale per la Scienza e Tecnologia dei Materiali (INSTM), Local Unit Università di Modena e Reggio Emilia, Italy

[3]SPCTS CEC, Université de Limoges UMR CNRS 7315, 12 Rue Atlantis 87060 Limoges CEDEX, France

[4]CEA Le Ripault, Laboratoire de Projection Thermique, B.P. 16, 37260 MONTS, France

[*]Corresponding author: tel. 0039 0592056233; fax: 0039 0592056243; giovanni.bolelli@unimore.it

Abstract

A novel plasma-spray process, featuring simultaneous injections of dry powders and multiple liquid streams, was employed to produce composite coatings where sub-micrometric particles of Al_2O_3 and hexagonal BN (*h*-BN) are dispersed within a NiCrAlY metal matrix. Various coatings, containing up to ≈10 wt.% Al_2O_3 and ≈9 wt.% *h*-BN, were obtained. A co-deposition effect was noted whereby a higher *h*-BN feed also increases Al_2O_3 incorporation in the coating, even under a constant flow rate of Al_2O_3 suspension.

Although the microhardness (≈600 $HV_{0.3}$) seemed rather insensitive to the composition of the coatings, their sliding wear resistance (tested under ball-on-disk configuration against corundum spheres at various temperatures) improved with increasing contents of Al_2O_3 and *h*-BN. The

improvement was more significant at room temperature, but some beneficial effect also emerged when testing at 400 °C and 700 °C. Al_2O_3 and *h*-BN indeed promote the formation and enhance the mechanical stability of an oxide-based tribofilm, protecting the coating surface from direct contact with the counterbody. Specific tribofilm formation mechanisms however vary with temperature. Overall, coatings containing ≥5wt.% of Al_2O_3 and *h*-BN keep a reasonably stable wear rate ($<5*10^{-4}$ $mm^3/(Nm)$) over a wide temperature range.

Key-words: Thermal spray coatings; Metal-matrix composite; Wear testing; Sliding wear; High temperature.

1. Introduction

Thermal spraying with liquid feedstock (suspensions or solutions) is one of the most promising, recent developments for the production of finely structured coatings [1–3]. It allows for the fast deposition rates typical of thermal spray processes in comparison to many other surface engineering technologies, and it is amenable for industrial scale-up [4]. Accordingly, some liquid feedstock spraying systems have recently become commercially available [5].

More specifically, a suspension feedstock allows delivering sub-micrometric or nanometric powder particles into a thermal spray gas stream using the liquid dispersion medium as a carrier, thus overcoming the limitations inherent to dry feeding of fine powders. The strong surface interactions between the particles would indeed cause flowability issues, whilst their extremely low inertia would hinder their entrainment inside the gas jet [2,3,6].

Suspension thermal (plasma or HVOF) spraying has therefore been proposed for the deposition of a variety of ceramic coatings, as reviewed e.g. in [1]. To the contrary, it has not been so frequently employed to process metals (few examples being given in [7,8]), as the high specific surface of fine metallic particles would result in extensive oxidation once the thermal spray gas stream mixes with the surrounding air.

In some applications, such as high-temperature wear protection, however, metal-matrix nanocomposite coatings reinforced by fine ceramic particles would be better suited than pure ceramic ones. The metal matrix would provide toughness, ensure sufficiently strong bonding to ordinary metallic substrates (such as steels and superalloys), protect them from oxidation, and match the respective thermal expansion coefficients, whilst the ceramic reinforcement would improve the wear resistance of the system.

"Hybrid" thermal spray processes using dual injection of distinct feedstock types have therefore been proposed [9–13]: the metallic powder is fed in dry form, whereas the fine ceramic reinforcement is delivered as a suspension (e.g. using a liquid carrier). For instance, a Mo-containing Ni-based alloy matrix reinforced by ceramic particles (e.g. ZrO_2) was reported in [11–13].

In a very recent study [14], the authors described the use of one such "hybrid" thermal spray techniques for the production of NiCrAlY+Al_2O_3 composite coatings. A dry NiCrAlY powder and a suspension of sub-micrometric Al_2O_3 particles were simultaneously delivered into the gas stream issuing out of a three-cathode plasma spray torch, using two distinct injection nozzles, each designed to handle the respective feedstock type. The coatings reportedly [14] exhibited good ball-on-disk sliding wear performances over a wide temperature range (from room temperature to 700 °C). The Al_2O_3 particles, pulled out of the coating surface at the early stages of the sliding contact, indeed promoted the early formation of a tribofilm at room temperature, protecting the metal matrix from adhesive wear. At 400 °C and at 700 °C, on the other hand, the metal matrix itself was able to develop a stable, oxidised "glaze" layer providing relatively low wear.

In the present paper, this concept has been developed further to the production of ternary coating formulations, comprising a NiCrAlY metal matrix, a sub-micrometric Al_2O_3 reinforcement, and a finely dispersed solid lubricant, capable of retaining its properties up to elevated temperatures. The goal is to induce a progressive release of solid lubricant particles during sliding contacts. The solid lubricant should therefore be smeared onto the mating surfaces, together with fragments of Al_2O_3

(as mentioned previously [14]), enhancing the tribofilm formation ability and improving the tribological performances of the system.

The incorporation of lubricants within coatings, and within thermal spray coatings in particular, has long been the subject of active research [15–19], leading to cutting-edge solutions such as the embedment of polymeric capsules containing a liquid lubricant inside flame-sprayed ceramic and metal coatings [20–22]. Specifically, the use of a liquid feedstock to deliver a solid lubricant during plasma spray deposition of wear-resistant coatings has first been proposed in the early work by Cipri et al. [9]. In that case, a "simpler" binary system with a pure Al_2O_3 matrix was employed and the lubricant consisted of graphite flakes. Graphite is however unsuitable for sustained operation at high temperatures, which is one of the goals of the present study. Hexagonal boron nitride (hereafter designated as *h*-BN) has therefore been selected in the present work, since it is a well-known high-temperature solid lubricant [23,24], reportedly capable of resisting oxidation up to ≈1000 °C even in nanoparticle form [25]. Moreover, due to its intrinsic brittleness, the ceramic matrix employed in [9] was highly sensitive to the defects introduced by the embedded graphite flakes, so that, even though the friction coefficient (tested in block-on-ring configuration) decreased, the wear rate reportedly increased, compared to that of an unreinforced alumina coating [9].

Ternary systems, where a metal matrix embeds both the hard phase and the solid lubricants in order to provide cohesion and toughness, have been under development for several decades. The foremost example is a series of plasma spray-grade powder blends consisting of a Ni-based alloy (e.g. Ni-Cr or Ni-Mo-Al alloys), a hard phase (glass, Cr_3C_2 or Cr_2O_3), Ag (as low-temperature lubricant) and eutectic CaF_2-BaF_2 (as high-temperature solid lubricant) [26–31]. These materials, developed by NASA, have been primarily employed as high temperature tribological coatings onto foil bearings operating in dry conditions at high temperatures.

The "hybrid" plasma spray process now offers the opportunity to obtain a much more finely structured coating than it was possible in the mentioned studies [26–31], with smaller, more widespread reinforcement and solid lubricant particles to enhance their tribological effectiveness.

The novelty of this study over all of the cited literature [9,26–31] (including the authors' own previous research [14]) therefore resides in the use of three distinct feedstock streams, simultaneously delivered into an atmospheric DC thermal plasma jet through separate injection ports. A conventional, dry NiCrAlY powder, a suspension of sub-micrometric Al_2O_3 particles and another one containing sub-micrometric *h*-BN particles were employed for this purpose, as each constituent is thermally stable and oxidation-resistant up to high temperatures (at least 900 – 1000 °C). The coatings are therefore suitable to provide wear protection over a wide temperature range, as it occurs in components experiencing running in at low temperatures and subsequent, prolonged operation at higher temperatures. Examples are shafts and journal bearings in industrial and aeronautic gas turbines, valve heads and piston rings in automotive applications, nuclear power plant components, etc.

2. Experimental

2.1 Feedstock materials

The chosen feedstock materials comprise:

- A Ni – 22%Cr – 10%Al – 1%Y (values in wt.%) gas-atomised powder (AMDRY 9624, Oerlikon-Metco, Wohlen, Switzerland) with -37+11 μm nominal particle size distribution;
- A sub-micrometric Al_2O_3 powder with d_{50} = 300 nm (AKP30, Sumitomo Chemicals Co., Japan);
- A sub-micrometric *h*-BN powder with d_{50} = 500 nm (MK Impex, Canada).

The Al_2O_3 and *h*-BN powders were dispersed in ethanol medium in order to enable liquid-carrier feeding into the plasma plume. Ethanol was selected because, compared to water, it favours better fragmentation of liquid drops (because of its lower surface tension) [32] and prevents excessive

plasma cooling. Not only it possesses lower vaporisation enthalpy, but it also reacts with the O_2 entering the plasma stream upon mixing with the surrounding air [33,34]. Preliminary tests showed that suspensions simultaneously containing Al_2O_3 and *h*-BN were not sufficiently stable: significant sedimentation indeed occurred within 30 min after dispersion. Distinct suspensions were therefore produced. Specifically, a suspension containing 10 wt.% Al_2O_3 powder and a series of suspensions containing 0 wt.% (pure ethanol), 1.25 wt.%, 2.5 wt.% and 5 wt.% *h*-BN were produced (see Table 1). In all cases, 2 wt.% Beicostat C213 was added as dispersant.

2.2 Coating deposition procedure

A TriplexPro-200 plasma spray torch (Oerlikon-Metco), featuring three cathodes and a segmented, annular anode nozzle, was employed. Compared to conventional plasma torches, it provides a more stable plasma flow [35], free of the typical oscillations that are particularly undesirable for the processing of liquid feedstock [36], and it allows for higher feedstock throughput with multiple injection points [37].

Table 1: summary of the tested samples with respective feeding conditions.

	Sample designation	**NiCrAlY feed rate (g/min)**	**Solid content (wt.%) in suspension feedstock (30 mL/min overall flow rate)**	
			Al_2O_3 suspension	**h-BN suspension**
Series 1	Ny10Al10BN0	10	10	0
	Ny10Al10BN1.25			1.25
	Ny10Al10BN2.5			2.5
	Ny10Al10BN5			5
Series 2	Ny20Al10BN0	20	10	0
	Ny20Al10BN1.25			1.25
	Ny20Al10BN2.5			2.5
	Ny20Al10BN5			5

Table 2: Plasma spray parameters.

Parameter	**Setting**
Anode nozzle diameter (mm)	6.5
Current (A)	450

Voltage (V)	103
Argon gas flow rate (SLPM)	70
Plasma enthalpy (MJ/kg)	13
Standoff distance (mm)	70
Powder flow rate (g/min)	10 – 20
Suspension flow rate (mL/min)	≈ 30

The torch, operated with the parameters summarised in Table 2, was equipped with two distinct injection ports. One was connected to a standard dry powder feeder (using a gas carrier), loaded with the NiCrAlY feedstock. The other one, consisting of a sapphire nozzle with an orifice diameter of 150 μm, was connected to a liquid delivery system comprising two pressurised vessels. Each contained separate suspensions of Al_2O_3 and *h*-BN (respectively), as described in Section 2.1 and listed in Table 1. An additional vessel was loaded with a flushing medium to clean the liquid feed line after spraying. The distinct Al_2O_3 and *h*-BN suspension streams were mixed together through a hydraulic circuit and conveyed to the liquid injection port.

Specifically, the flow rates of the Al_2O_3 and *h*-BN suspensions were kept constant, and eight distinct samples were obtained by coupling a low and high NiCrAlY powder feed rate with the four different *h*-BN suspensions containing 0 wt.% (pure ethanol), 1.25 wt.%, 2.5 wt.% and 5 wt.% of powder (Table 1). The aim was to obtain a variety of coatings having a sufficiently wide range of proportions between the NiCrAlY, *h*-BN and Al_2O_3 constituents, in order to study the relation between composition and tribological behaviour.

2.3 Structural, microstructural and chemical characterisation methods

Cross-sectional samples, prepared by metallographic cutting, were embedded in room temperature-setting epoxy resin, ground with SiC papers (up to 2500 mesh) and polished with 3 μm diamond suspension and colloidal silica slurry. These polished sections were observed by field emission gun-scanning electron microscopy (FEG-SEM: Nova NanoSEM 450, FEI, Eindhoven, The Netherlands) equipped with energy-dispersive X-ray (EDX) microanalysis probe (Quantax-200, Bruker).

Depth-sensing Berkovich micro-indentation testing (Micro-Combi Tester, Anton-Paar TriTec, Peseux, Switzerland) was also performed on the polished sections, with a 3 N maximum load, 4.5 N/min loading/unloading rate, and 15 s load holding time. Tests and depth-sensing data analysis were carried out in accordance with the relevant ISO standards [38–40].

The top surface of the samples, ground and polished to Ra ≈ 0.02 μm according to the same procedure described above, were employed for X-ray diffraction (XRD) analysis (X'Pert PRO, PANAlytical, Almelo, The Netherlands). XRD patterns were acquired over the $2\theta = 20° – 100°$ angular range, with a scanning step of 0.017° and an acquisition time of 90 s/step, using Cu-Kα radiation, monochromatised through an X-ray mirror and collected in a 1D-solid state detector.

Micro-Raman spectroscopy (LabRam, Horiba Jobin-Yvon, Longjumeau, France) was also carried out on polished top surfaces in order to determine the structure of the ceramic phases (oxides, nitrides) contained in the coating. Most spectra were acquired using a 532.05 nm-wavelength laser, focused through a 100x objective; additional spectra were acquired with a 632.81 nm-wavelength laser focused through the same objective.

The Al_2O_3 content of the coatings was determined by X-ray fluorescence (XRF: ARL SMS-Omega, Thermo Scientific, Waltham, MA, USA) on two samples for each of the eight coating types, according to the procedure previously described in [14]. Briefly, the amounts of Ni and Al in the coatings are measured by XRF and the Al/Ni ratio is compared to the nominal value of the NiCrAlY feedstock. Assuming that elements were not vaporised to a substantial extent from the NiCrAlY metal matrix during plasma spraying, the excess Al (compared to the Al/Ni ratio of the feedstock powder) is due to the incorporation of Al_2O_3. The amount of the latter is therefore computed through the ratio of the molecular mass of Al_2O_3 to the atomic mass of Al.

Similarly, the *h*-BN content was determined (on two samples for each coating) using an inductively coupled plasma – mass spectrometer (ICP – MS: X Series^{II}, Thermo Fischer Scientific, Waltham, MA, USA) coupled to a laser ablation (LA) system (New Wave UP 213). The laser was scanned along five stripes of 500 x 65 μm size on the polished top surface of the samples (ultrasonically

cleaned in acetone and further cleaned by a low-power laser pre-ablation scan) to vaporise the coating material. A flow (600 SL/h) of He carries the vapours into the RF-inductively coupled plasma torch, where elements are ionised. Ions are separated based on their mass/charge ratio and analysed through the downstream quadrupole mass spectrometer. In order to obtain quantitative measurements, reference samples of known chemical composition were simultaneously analysed and employed to build calibration curves relating the MS signal intensity to actual element concentrations. Specifically, a pure (99.999%) Ni foil, a Nimonic alloy foil (20,0wt.% Cr, 18,0wt.%Co, 1.5wt.% Al, 1,5wt.%Fe, bal. Ni) and a Ni-17%Si-14%B sheet were analysed to build calibration curves for Ni and B. The actual amount of B (in wt.%) is therefore computed. Assuming that B comes entirely from *h*-BN, the mass of the latter is computed from the ratio of its molecular mass to the atomic mass of B (the actual presence of *h*-BN in the samples is ensured by micro-Raman spectra as later shown in Section 3.1).

2.4 Sliding wear test method

Sliding wear tests were carried out in ball-on-disk configuration according to the ASTM G99 standard (High Temperature Tribometer, Anton Paar TriTec). The significance of this test is to provide a comparative screening among a variety of materials [41]; its acceptance is testified e.g. by its use in order to build wear maps providing a widespread reference for the engineering practice [42]. This test has accordingly been employed by various authors to characterise the tribological behaviour of metallic and composite materials, including thermal spray coatings [43–49]. Most importantly, the same test has been employed by the authors in the previous study on NiCrAlY+Al_2O_3 coatings [14], as well as on other metal and hardmetal coatings [50]; hence, there is large availability of comparative data acquired under identical experimental conditions.

Sample surfaces were ground and polished to Ra ≈ 0.02 μm as described in Section 2.3, and ultrasonically cleaned in acetone before each test. Sintered Al_2O_3 spheres were employed as stationary counterbody. Al_2O_3 retains hardness and phase stability up to high temperatures, and its

chemical inertness helps preventing the occurrence of additional tribochemical interactions, which would complicate the interpretation of the wear mechanisms by masking the coatings' own response, as already explained in [14].

Test conditions are summarised in Table 3. Most importantly, tests were run at three temperatures (room temperature, 400 °C, 700 °C). In high temperature tests, the rotating support plate was induction heated and the temperature of the sample was monitored with a thermocouple in contact with its rear face. Heating to the prescribed temperature lasted 1 h; the sample was then kept in isothermal conditions for 40 min before sliding contact was started, in order to ensure that a homogeneous temperature was achieved throughout its thickness. Samples were therefore maintained at the prescribed temperature for an overall duration of about 6 h 35 min inside the tribometer. All tests were run in replicate.

The friction coefficient was monitored continuously during the test by measuring the tangential force through a load cell attached to the ball-holding arm.

Table 3: ball-on-disk test conditions

Counterpart (sphere) material	Sintered Al_2O_3
Counterpart (sphere) diameter	6 mm
Normal load	5 N
Relative sliding speed	0.1 m/s
Wear track radius	5 mm
Relative sliding distance	2000 m
Temperatures	Room temperature (≈25 °C) 400 °C 700 °C

Wear was expressed in terms of volume loss (V), assessed by scanning confocal profilometry (CHR150 profilometer, STIL, Aix-en-Provence, France) on the sample and by optical microscopy (in order to measure the diameter of the removed hemispherical cap) on the counterbody. Volume loss values were converted to wear rates (K) by normalising over the applied load (P) and the relative sliding distance (l): $K = V/(P \cdot l)$.

The surfaces and cross-sections of worn samples (the latter prepared by cold-mounting in epoxy resin before metallographic cutting, in order to avoid artificial damage to the wear scar) were observed by FEG-SEM; the phase composition of heated samples was characterised by XRD and further structural analyses were carried out on worn surfaces by micro-Raman spectroscopy. Moreover, chemical analyses by ICP-MS + LA were performed inside the wear tracks on the samples in order to verify the presence of boron. All of these tests were carried out under the same experimental conditions as described in Section 2.3.

3. Results and discussion

3.1 Structural and microstructural analyses

The general microstructural features of the present coatings, as seen in Figs. 1 and 2, are consistent with those previously reported by the authors for "hybrid" plasma sprayed NiCrAlY + Al_2O_3 [14]. Specifically, the coatings are macroscopically homogeneous and free from large-scale defects: Fig. 1 shows representative micrographs of some of the samples studied in this work. Their thickness is roughly comprised in the ~300 – 450 μm range. Their "backbone" consists of the superposition of a large number of NiCrAlY lamellae with various degrees of flattening, reflecting the different impact temperatures and velocities of distinct particles, which is typical of plasma-sprayed coatings [51,52]. Different thermal histories also result in a variety of intralamellar structures (Fig. 2A), ranging from fine columnar crystals to fine and coarse equiaxed crystals (better seen in the magnified view of Fig. 2B). Unmolten particles, retaining the dendritic/cellular microstructure of the gas-atomised NiCrAlY feedstock (previously characterised in [14]) are also visible (Fig. 2C). A few, irregularly shaped pores (Fig. 1: arrows) presumably originate from voids left between incompletely flattened lamellae [51].

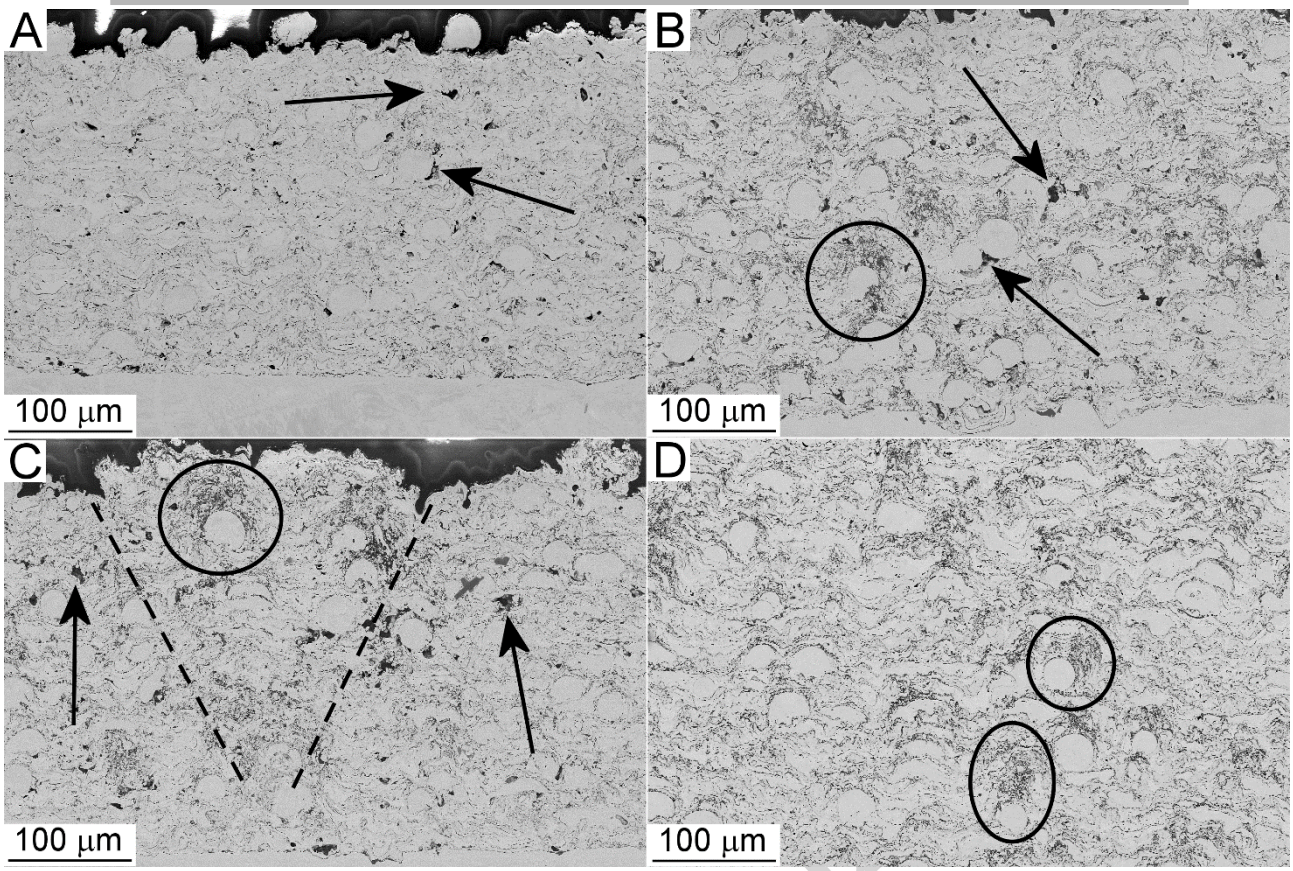

Figure 1. Cross-sectional SEM micrographs (backscattered electrons mode) of samples Ny10Al10BN0 (A), Ny10Al10BN1.25 (B), Ny10Al10BN2.5 (C) and Ny20Al10BN2.5 (D). Arrows indicate pores, circles indicate clustering of sub-micrometric Al_2O_3 and *h*-BN particles around non-flattened NiCrAlY particles, and dashed lines mark a cone-shaped defect.

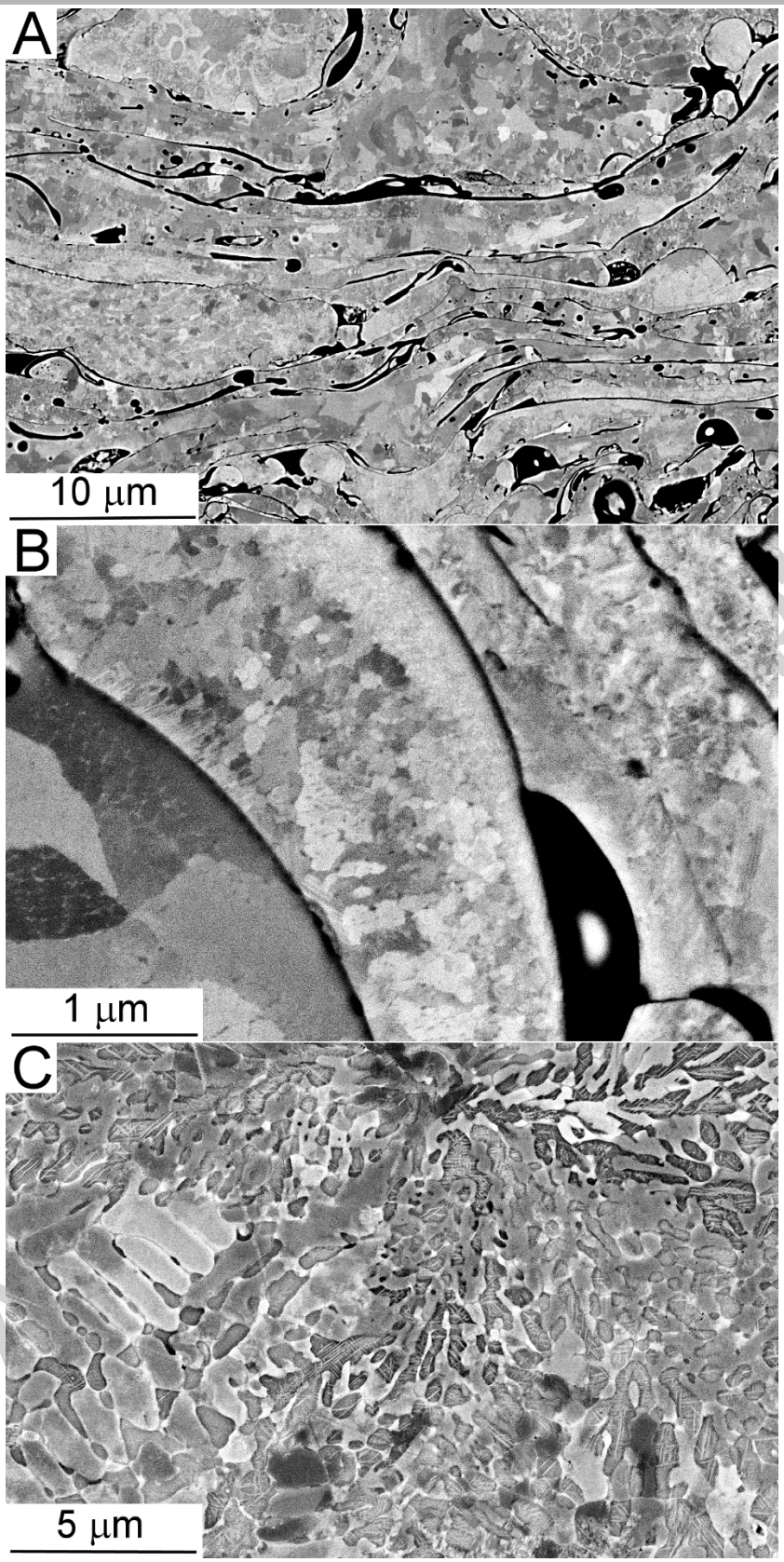

Figure 2. High-magnification cross-sectional SEM micrographs (backscattered electrons mode) showing the NiCrAlY grain structure in sample Ny10Al10BN0: flattened lamellae (A,B) and non-flattened particle (C).

The main phase of the metal alloy matrix is a solid solution based on γ-Ni and/or γ'-Ni_3Al, with little β-NiAl (see the XRD patterns in Fig. 3A), as the precipitation of the latter inside molten lamellae was hindered by the generally high cooling rates.

The diffraction peaks of Al_2O_3 and *h*-BN, as well as those of inclusions produced by oxidation of the NiCrAlY matrix during spraying, can hardly emerge from the strong background signal produced by the Ni-based alloy (as previously noted in [14]), except for a very weak peak belonging to γ-Al_2O_3 (Fig. 3A). This metastable phase is typically formed in thermally-sprayed alumina due to the rather high cooling rate of molten ceramic droplets [53]. Accordingly, molten Al_2O_3 particles, with a characteristic rounded shape, are clearly seen in magnified cross-sectional views (Fig. 4A), their chemical composition being confirmed by EDX spectra (Fig. 4C – spectrum 4). The rounded shape is due to the low impact velocity of such fine, low-inertia particles, which prevents them from flattening [54]. They can be distinguished from elongated, interlamellar inclusions produced by oxidation of NiCrAlY splats (Fig. 4A,C: spectrum 2), which are richer in Ni and Cr.

Micro-Raman spectroscopy allows focussing onto these non-metallic phases with a micrometre-sized lateral resolution. It reveals a rather broad peak at 545 cm^{-1}, ascribed to NiO [55,56] and/or Cr_2O_3 [55,57–59], a band at about 1090 cm^{-1}, also belonging to NiO [56], and a broad peak at 690 cm^{-1}, indicating the presence of $NiCr_2O_4$-type spinel oxides [56,59,60] (Fig. 3B).

When *h*-BN is fed into the plasma jet, irregular particles rich in B and N (Fig. 4A and EDX spectrum in Fig. 4C – spectrum 3) are also found: they generate the darkest backscatter electrons contrast level (also see the features marked in Fig. 4B). They presumably correspond to unmolten *h*-BN inclusions; indeed, the Raman spectra of the corresponding coatings (see for instance the spectrum of sample 4 in Fig. 3B) exhibit its characteristic, sharp peak at about 1350 cm^{-1} [61,62]. As mentioned in the introduction, *h*-BN is highly resistant to oxidation; hence, unmolten particles could be embedded within the coatings without significant oxidation (apart from a likely thin shell

on their outer surface). Indeed, none of the Raman spectral features of B_2O_3, as described e.g. in [63,64], is identifiable.

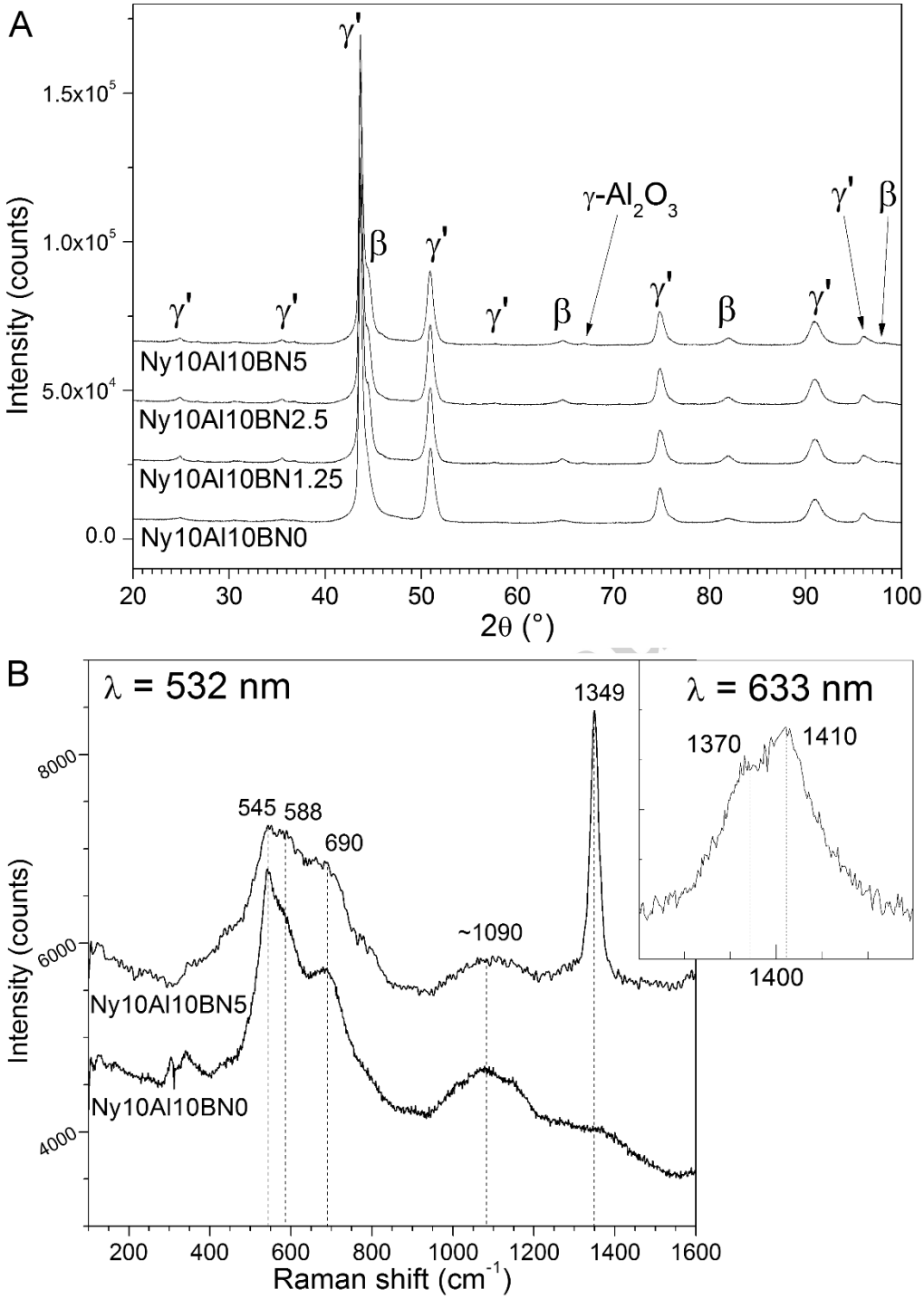

Figure 3. (A) Representative XRD patterns of selected coatings, and (B) representative micro-Raman spectra acquired on non-metallic inclusions of samples Ny10Al10BN0 and Ny10Al10BN5 using a "green" (λ = 532 nm) laser. The inset shows a detail of the spectrum acquired on sample Ny10Al10BN5 with a "red" (λ = 633 nm) laser.
Legend of panel A: γ' = γ'-Ni_3Al (JCPDF 3-65-140); β = β-NiAl (JCPDF 3-65-431); γ-Al_2O_3 (JCPDF 10-425).

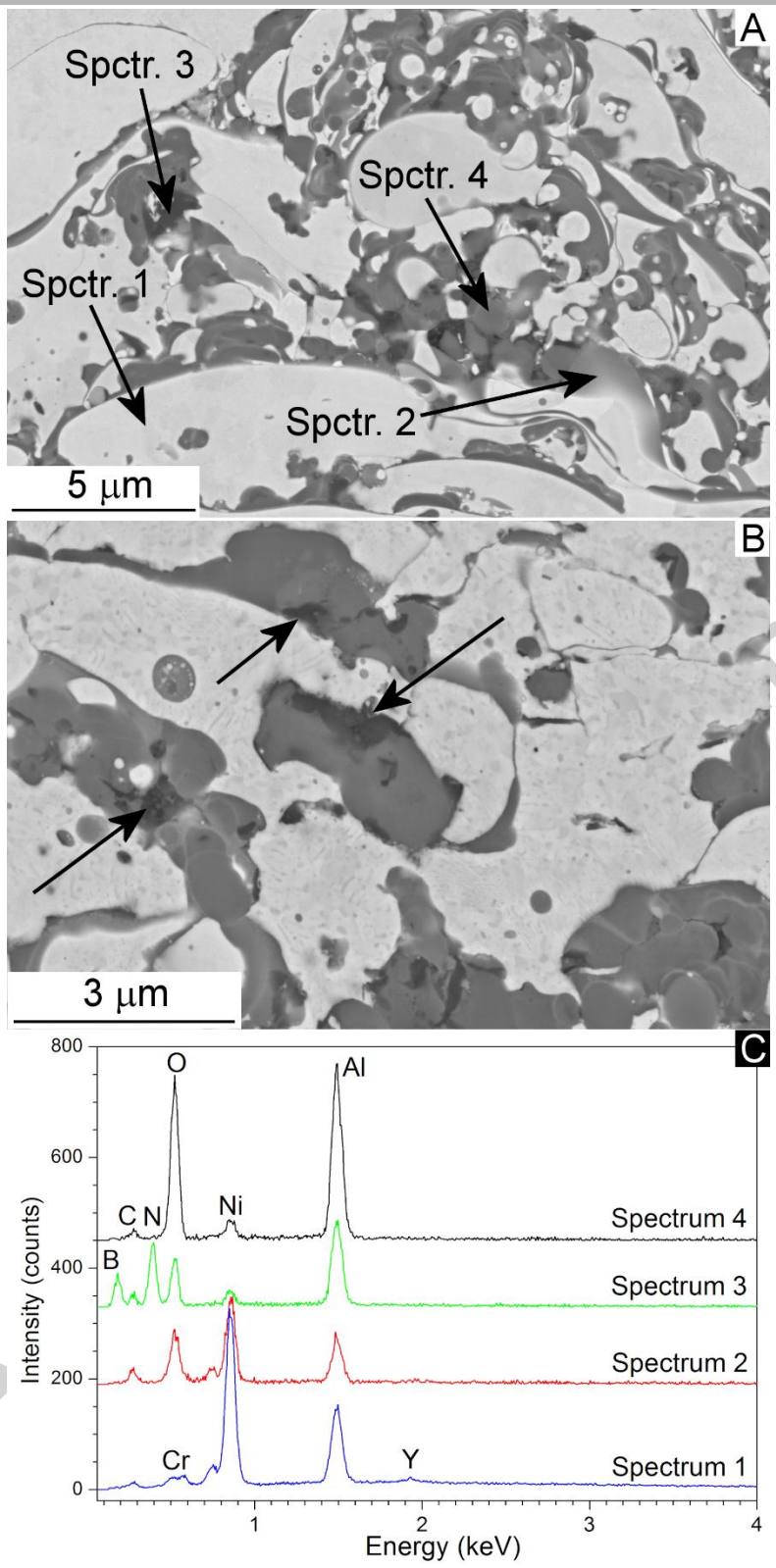

Figure 4. Cross-sectional SEM micrographs (backscattered electrons mode) showing details of the non-metallic inclusions in sample Ny10Al10BN5 (A,B), and corresponding EDX spectra acquired at the locations labelled in panel A, with 8 keV electron beam energy (C).
In panel B, the arrows indicate some of the recognisable *h*-BN inclusions.

The γ-Al_2O_3 structure has no Raman-active mode [65], but the presence of Al_2O_3 within the coatings is anyway reflected by exciting its photoluminescence emission through a 632 nm-wavelength (red colour) laser. A characteristic doublet at wavenumbers of about 14430 cm^{-1} and 14400 cm^{-1} [66,67] is indeed produced, which overlaps with the Raman spectrum produced by the "red" laser at wavenumber shifts of 1370 cm^{-1} and 1410 cm^{-1} (see inset in Fig. 3B). Obviously, this strong emission covers the Raman signal itself; hence, the "red" laser would have been unsuitable to reveal the presence of *h*-BN.

Chemical analyses carried out by XRF and by ICP-mass spectrometry coupled to laser ablation (as described in Section 2.3) show that, when *h*-BN is fed into the plasma, the amount of Al_2O_3 in the coatings is higher, although its feed rate was kept constant throughout all of the experiments (Table 4). Low-magnification cross-sectional SEM micrographs qualitatively confirm that, when no *h*-BN is fed, the overall amount of sub-micrometric particles within the coating is much lower (compare Fig. 1A to Figs. 1B-D). The detailed views of Fig. 4A,B confirm that Al_2O_3 and *h*-BN particles often lay adjacent to one another. There is, therefore, a tendency towards co-deposition of these two types of sub-micrometric particles, although the relation between the amount of Al_2O_3 and of *h*-BN (Table 4) is not exactly linear.

A detailed, fundamental investigation of this phenomenon is outside the scope of this work, which primarily aims to study the sliding wear behaviour of the samples in relation to their microstructure and composition, but the hypothesis is proposed that co-deposition arises from the similarities of the trajectories followed by these light particles in the plasma jet. As thoroughly illustrated in [54], sub-micrometric particles, having low inertia (Stokes number $St<1$), are affected by the stagnation flow in front of the substrate surface. Consequently, they slow down and deflect along trajectories parallel to that surface, thus attaching preferentially to prominent asperities. Clustering of fine particles (Fig. 1B-D: see the circled areas) is indeed often seen to occur in correspondence to non-flattened, unmolten NiCrAlY particles, which stand proud of the surrounding material in the growing layer. The locally higher deposition rate of fine particles sometimes results in the

expansion of fast-growing "cones" (see dashed lines in Fig. 1C). These are typical of thermally sprayed coatings obtained from liquid feedstock [34,54,68,69], and were previously reported in the NiCrAlY+Al_2O_3 layers studied by the authors in [14]. Moreover, deposited particles may further promote the attachment of other ones by virtue e.g. of chemical affinity between Al_2O_3 and the extremely thin oxide shell that presumably surrounds the *h*-BN particles.

Table 4: summary of samples characterisation testing: content of Al_2O_3 (from XRF) and *h*-BN (from ICP-mass spectroscopy + laser ablation), indentation hardness and elastic modulus, sliding wear rates and friction coefficients from ball-on-disk testing.

		Series 1				**Series 2**			
Designation		Ny10 Al10 BN0	Ny10 Al10 BN1.25	Ny10 Al10 BN2.5	Ny10 Al10 BN 5	Ny20 Al10 BN0	Ny20 Al10 BN1.25	Ny20 Al10 BN2.5	Ny20 Al10 BN5
Al_2O_3 (wt. %)		1.09	8.40	5.96	9.68	1.09	1.25	8.06	2.03
h-BN (wt. %)		0	5.3	5.7	8.7	0	0.3	1.0	2.0
H_{IT} (GPa)		7.7 ± 0.3	6.2 ± 0.7	6.7 ± 0.9	6.5 ± 0.8	6.4 ± 0.5	6.9 ± 0.6	7.0 ± 1.0	8.0 ± 1.0
E_{IT} (GPa)		191 ± 6	171 ± 12	186 ± 15	181 ± 13	128 ± 8	207 ± 10	224 ± 14	170 ± 24
R.T.	*Wear rate [*10^{-5} mm^3/(Nm)]*	10.17 ± 1.16	1.41 ± 0.09	1.99 ± 0.19	1.07 ± 0.09	4.02 ± 0.50	6.86 ± 0.19	1.12 ± 0.41	5.65 ± 0.08
	Friction coefficient	0.68 ± 0.04	0.69 ± 0.04	0.68 ± 0.04	0.64 ± 0.05	0.66 ± 0.04	0.69 ± 0.04	0.69 ± 0.03	0.66 ± 0.04
400 °C	*Wear rate [*10^{-5} mm^3/(Nm)]*	2.93 ± 0.48	3.46 ± 0.47	3.06 ± 0.18	3.93 ± 0.13	2.05 ± 0.41	4.80 ± 0.83	3.72 ± 0.38	8.91 ± 0.42
	Friction coefficient	0.49 ± 0.05	0.58 ± 0.03	0.54 ± 0.05	0.59 ± 0.04	0.45 ± 0.06	0.52 ± 0.05	0.52 ± 0.05	0.56 ± 0.03
700 °C	*Wear rate [*10^{-5} mm^3/(Nm)]*	1.03 ± 0.56	0.49 ± 0.36	0.83 ± 0.52	3.83 ± 0.43	1.08 ± 0.80	1.26 ±0.67	0.49 ± 1.99	0.76 ± 0.61
	Friction coefficient	0.45 ± 0.02	0.50 ± 0.01	0.49 ± 0.01	0.52 ± 0.02	0.46 ± 0.03	0.47 ± 0.04	0.47 ± 0.01	0.48 ± 0.02

3.2 Tribological behaviour

3.2.1 Quantitative results from ball-on-disk testing

Wear rates and friction coefficients (average ± standard deviation) measured by ball-on-disk testing at various temperatures are listed in Table 4. The average wear rates at room temperature have a general tendency to decrease as the amount of Al_2O_3 and *h*-BN in the coatings increase, which is better seen in the 3D plot of Fig. 5A, where the wear rate of a pure NiCrAlY coating (taken from

[14]) is also added. With at least 5 wt.% of both Al_2O_3 and *h*-BN, the wear rates become lower than that of a HVOF-sprayed NiCrBSi-type self-fluxing alloy coating (tested in [50]) and approach that of a FeCrB-type alloy. Their values are presented as dashed lines on the *x*-*z* and *y*-*z* projections of the 3D plot in Fig. 5A. Wear rates, however, exceed that of HVOF-sprayed Cr_3C_2-NiCr (also taken from [50]) by one order of magnitude.

Due to the co-deposition effect mentioned in Section 3.1, the amounts of Al_2O_3 and *h*-BN increase together; hence, it is not possible to determine univocally which of the two types of particles has the biggest effect on wear rates. Better understanding is however gained by plotting the present data against those of the NiCrAlY + Al_2O_3 coatings (containing no *h*-BN) studied in [14] (Fig. 6A). The addition of *h*-BN seems beneficial when the reinforcement content is low, whilst all performances of the coatings with and without *h*-BN are levelled at high Al_2O_3 contents (Fig. 6A).

At 400 °C (Table 4 and Fig. 5B) and at 700 °C (Table 4 and Fig. 5C), the reinforcement phases become less influential. Nonetheless, a comparison to the NiCrAlY + Al_2O_3 coatings containing no *h*-BN [14] shows some improvement when increasing amounts of *h*-BN are added (Fig. 6B,C). Wear rates become similar to or even slightly better than those of Cr_3C_2-NiCr at the same temperatures, and definitely outperform NiCrBSi- and FeCrB-type alloy coatings (all data from [50]).

Overall, samples with at least 5 wt.% of Al_2O_3 and *h*-BN exhibit a rather stable wear rate over a wide temperature range, going from $K \approx 1*10^{-5}$ mm^3/(Nm) at room temperature to $K \approx 3.5*10^{-5}$ mm^3/(Nm) at 400 °C and $K \approx 0.5*10^{-5}$ mm^3/(Nm) at 700 °C (Table 4 and Fig. 5). With hardness values $H \approx 7$ GPa (Table 4), wear rates $K \approx 10^{-5}$ mm^3/(Nm) correspond to a dimensionless wear coefficient $K_{ad} \approx 7*10^{-5}$, where $K_{ad} = K \cdot H = (V \cdot H)/(P \cdot l)$ [70–72]. This value is below the severe wear threshold and can be classified as moderate wear, according to the review provided in [73].

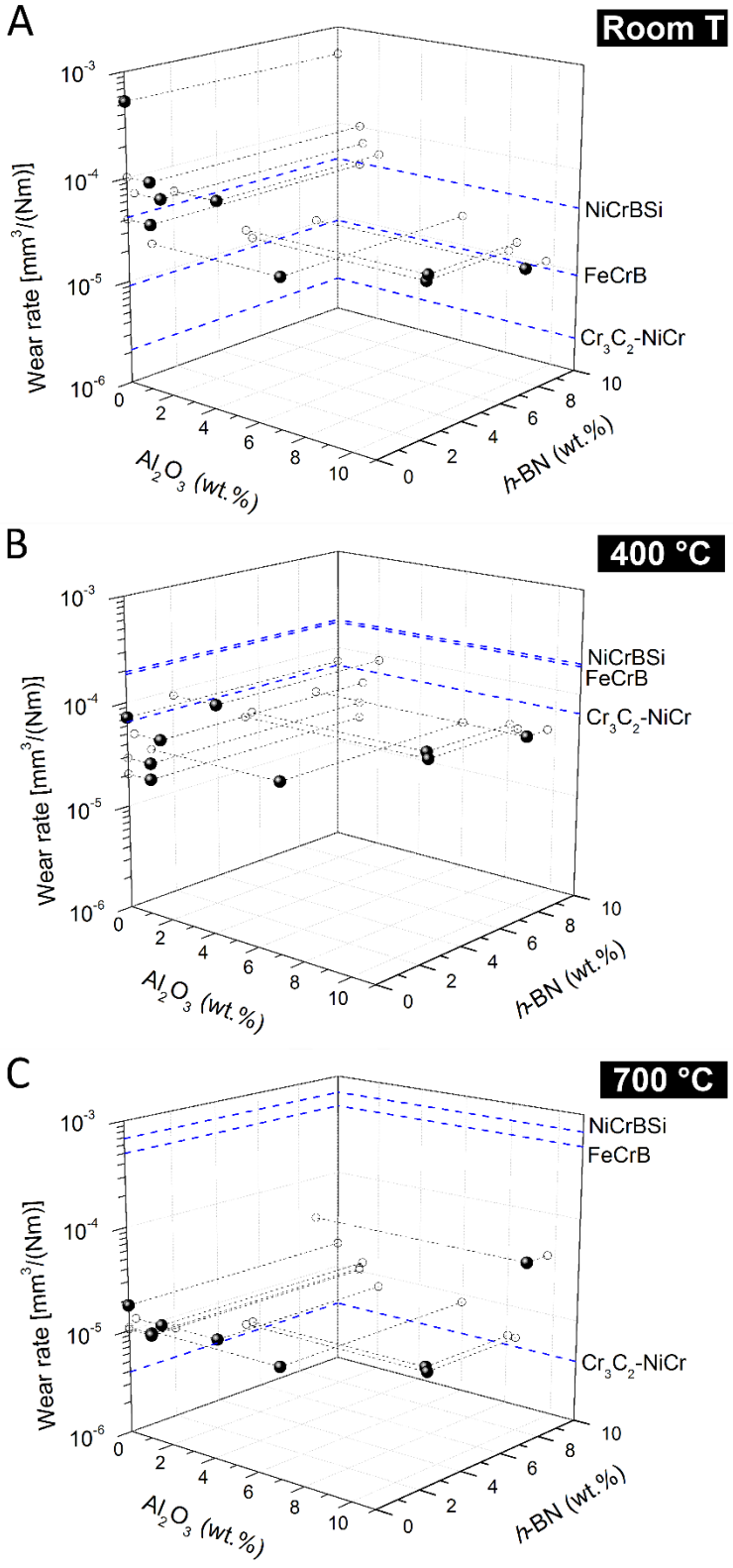

Figure 5. 3D plots showing the ball-on-disk wear rates of the coatings at (A) room temperature, (B) 400 °C and (C) 700 °C, as a function of the content of Al_2O_3 and *h*-BN. Projections of the plots on the *x*-*z* and *y*-*z* planes show the dependence of wear rates on the content of one type of particle only. Dashed lines on the projections indicate reference wear rates of HVOF-sprayed NiCrBSi, FeCrB-type alloy, and Cr_3C_2-25wt.%(Ni-20wt.%Cr), obtained under analogous test conditions in [50].

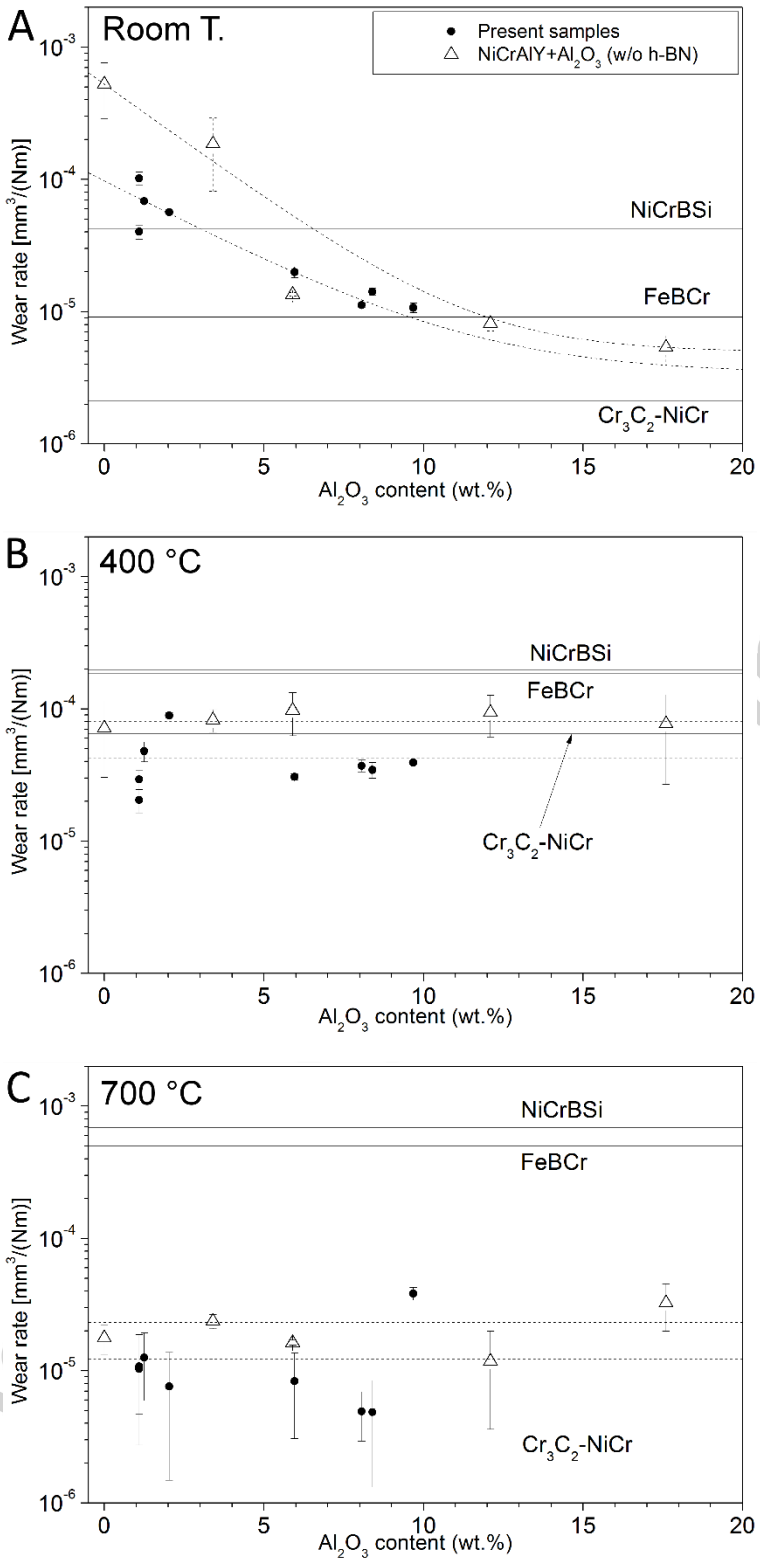

Figure 6. Comparison between the wear rates of the present samples (A: room temperature, B: 400 °C, C: 700 °C) and those of the NiCrAlY+Al_2O_3 samples tested in [14] under identical conditions, as a function of the Al_2O_3 content. Dashed lines provide guide-to-the-eye trends of the wear rates of the two series of samples. Solid lines indicate reference wear rates of HVOF-sprayed NiCrBSi, FeCrB-type alloy, and Cr_3C_2-25wt.%(Ni-20wt.%Cr), obtained under analogous test conditions in [50].

Such coatings are therefore suitable to protect components subject to sliding contacts at various temperatures, e.g. transitioning from a low-temperature start-up regime to high-temperature operation conditions. Examples, as also mentioned in the Introduction, are shafts and journal bearings in gas turbines, or valve heads and valve shafts in internal combustion engines. The particularly low wear rates at the highest test temperature of 700 °C is especially promising for this purpose.

3.2.2 Sliding wear mechanisms – room temperature

It is clear that the wear behaviour is not related to hardness, which indeed remains quite constant irrespective of the composition of the coatings (Table 4). Apart from hardness, many other factors affect the sliding wear behaviour of metals and composites [72], often having an even more important role.

SEM inspection of worn surfaces indicates that, at room temperature, the coatings develop a discontinuous tribo-layer ("tribofilm") made up of oxide clusters, clearly identifiable in backscattered electron contrast mode (Fig. 7A,B: see arrows).

The main effect of Al_2O_3 and *h*-BN is that of enhancing the tendency towards tribo-oxidation: the extension of tribofilm-covered surface in the wear scar grows with increasing amounts of Al_2O_3 and *h*-BN in the coatings (compare the scar of sample Ny10Al10BN0 – Fig. 7A – to that of sample Ny10Al10BN5 – Fig. 7B). The data in Table 4 and Fig. 5B,C clearly indicates that promoting tribo-oxidation is directly related to a decrease in wear rates. By mediating the contact between the mating bodies, the oxidised tribofilm clusters indeed reduce the associated phenomena of abrasive grooving and adhesive tearing on the coating surface. Evidence to the latter phenomena is visible on sample Ny10Al10BN0, containing only ≈1 wt.% Al_2O_3 and no *h*-BN, (Fig. 8A), as opposed to the behaviour of sample Ny10Al10BN5 (Fig. 8B), containing ≈10 wt.% Al_2O_3 and ≈9 wt.% *h*-BN.

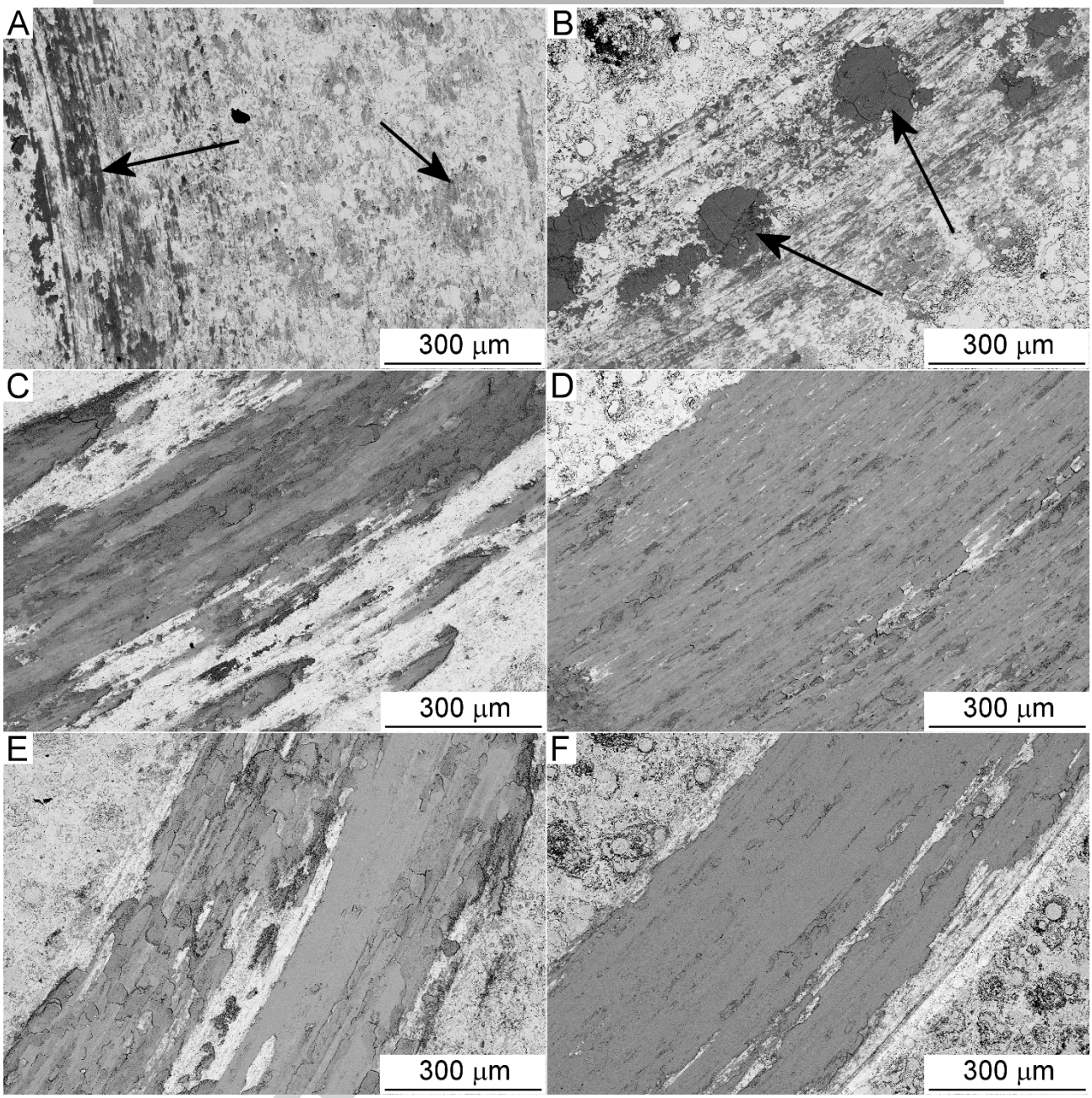

Figure 7. SEM micrographs of the wear scars produced by ball-on-disk testing on samples Ny10Al10BN0 (A,C,E) and Ny10Al10BN5 (B,D,F), at room temperature (A,B), at 400 °C (C,D) and at 700 °C (E,F).

The clusters consist of smeared patches of debris particles, including few larger, metallic fragments (most likely, lamellar debris from adhesive wear: Fig. 9A, label 1) within a matrix of sub-micrometric oxidised particles (see the details in Fig. 9B). Cross-sectional views confirm the discontinuous coverage of the surface by such patches (encircled in Fig. 10A), less than 1 μm thick (detail in Fig. 10B). TEM micrographs acquired on the loose fraction of such debris (collected on

the worn samples after the test) further testify to the presence of submicron- and nano-particles (Fig. 9C) with a partly crystalline structure. Lattice planes are seen in the high-resolution detail of Fig. 9D, and some diffraction spots and rings co-exist with a broad background halo due to a glassy phase in the related SAED pattern.

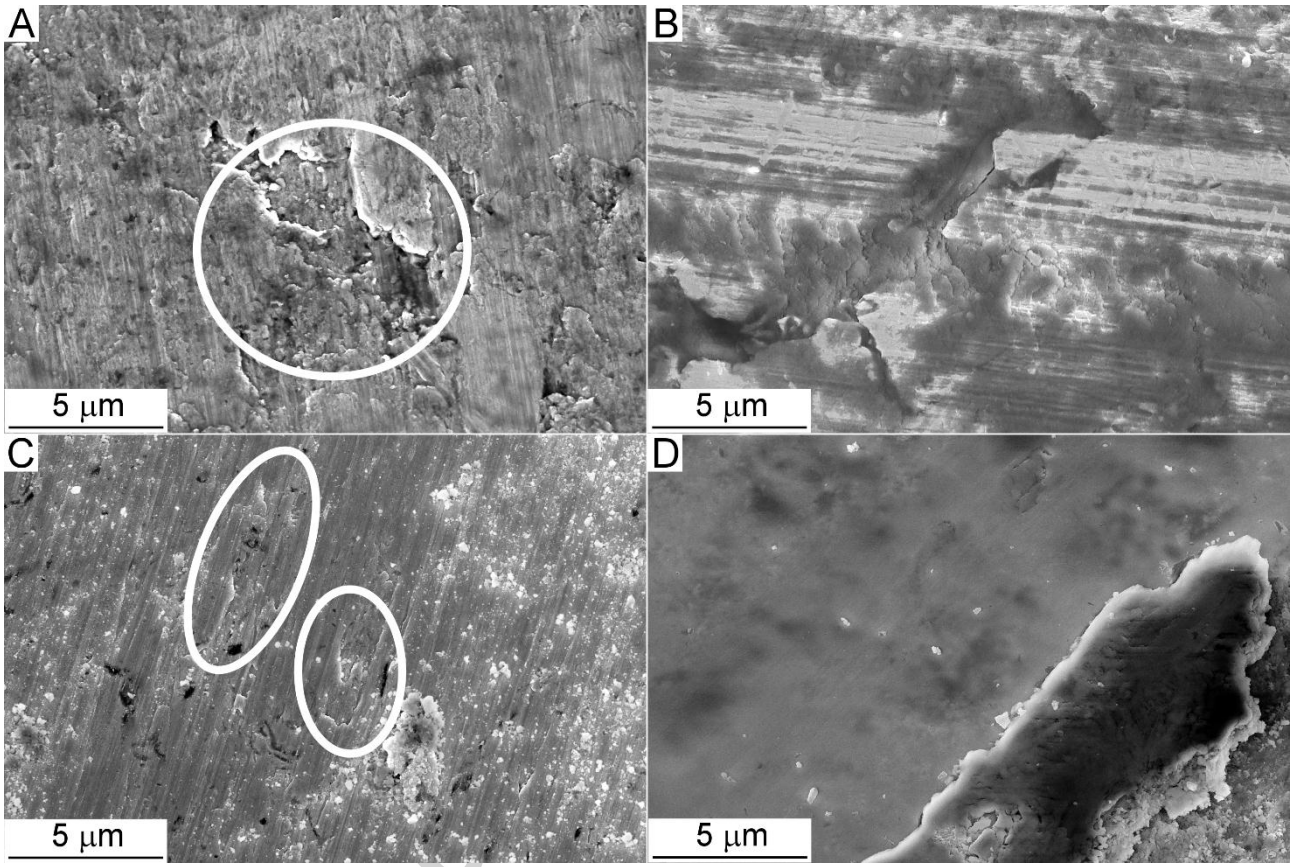

Figure 8. SEM micrographs showing details of abrasive grooving and adhesive tearing (occurrences of the latter are circled) on sample Ny10Al10BN0 after ball-on-disk wear testing at room temperature (A) and at 400 °C (C), compared to the wear scars on sample Ny10Al10BN5 at room temperature (B) and at 700 °C (D), showing coverage by different types of tribofilms.

The better tribo-oxidation ability of the Al_2O_3 and *h*-BN-rich coatings indicates that the initial "embryo" of the tribofilm probably originated from these same particles. Tribo-oxidised NiCrAlY debris was subsequently attached to the tribofilm, where indeed all the elements of that alloy can be found (see the EDX spectra of the oxidised tribofilm patches of samples Ny10Al10BN0 and Ny10Al10BN5 in Fig. 11A). EDX spectra cannot detect boron and nitrogen in the clusters, regardless of the composition of the coating, but ICP-mass spectrometry, being much more

sensitive to light elements, reveals variable amounts of boron when the laser ablation system is focussed onto the oxide clusters on *h*-BN-containing samples, ranging from few percent units to maxima of 10 wt.%.

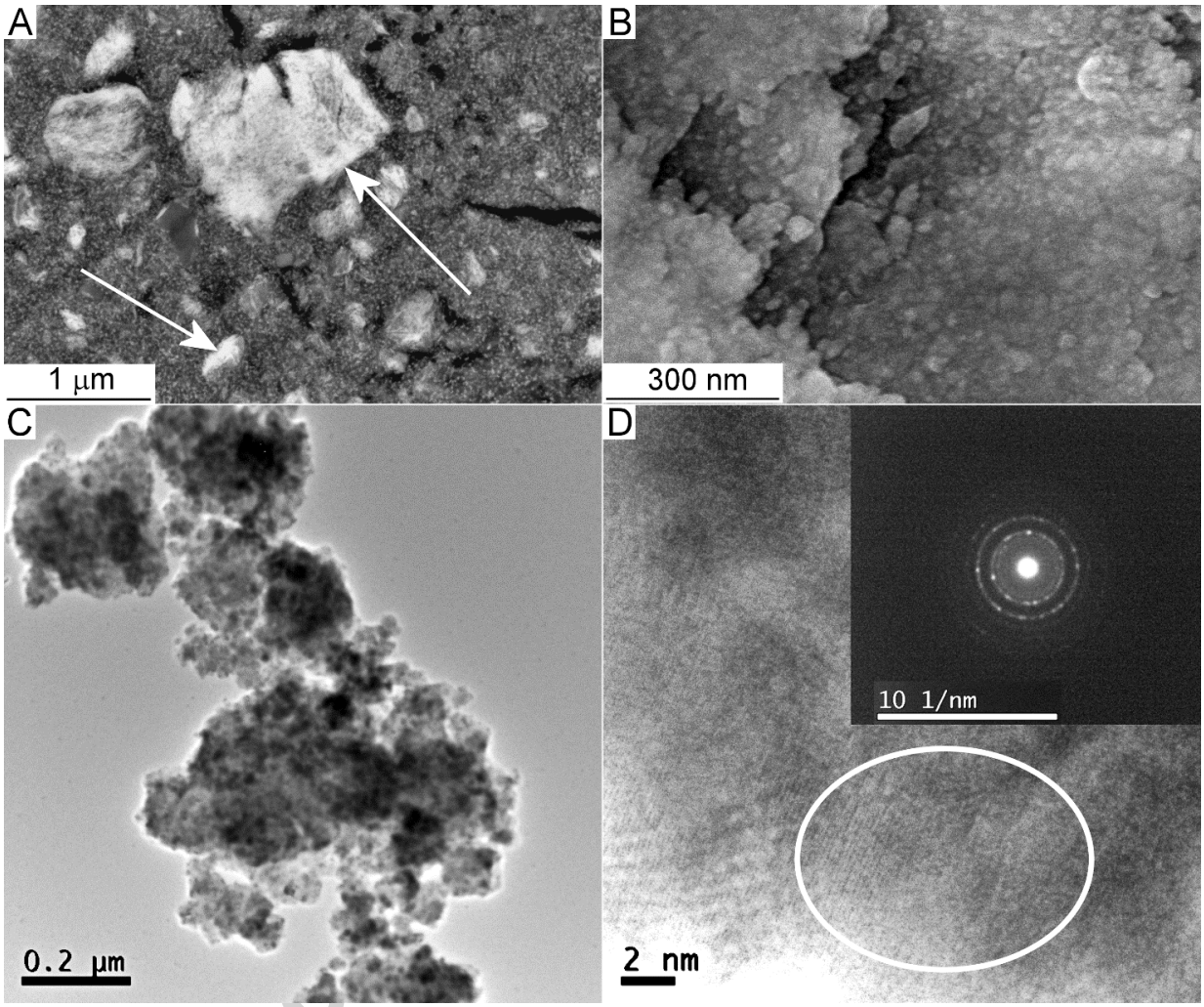

Figure 9. Wear debris generated by ball-on-disk wear testing of sample Ny10Al10BN5 at room temperature. A: backscattered electrons SEM micrograph of the smeared debris patches on the sample surface (arrows = metallic fragments); B: secondary electrons SEM detail of the same patches; C: TEM micrograph of loose debris particles; D: high-resolution TEM detail of the same, (circled area = lattice fringes), with inset selected area electron diffraction (SAED) pattern.

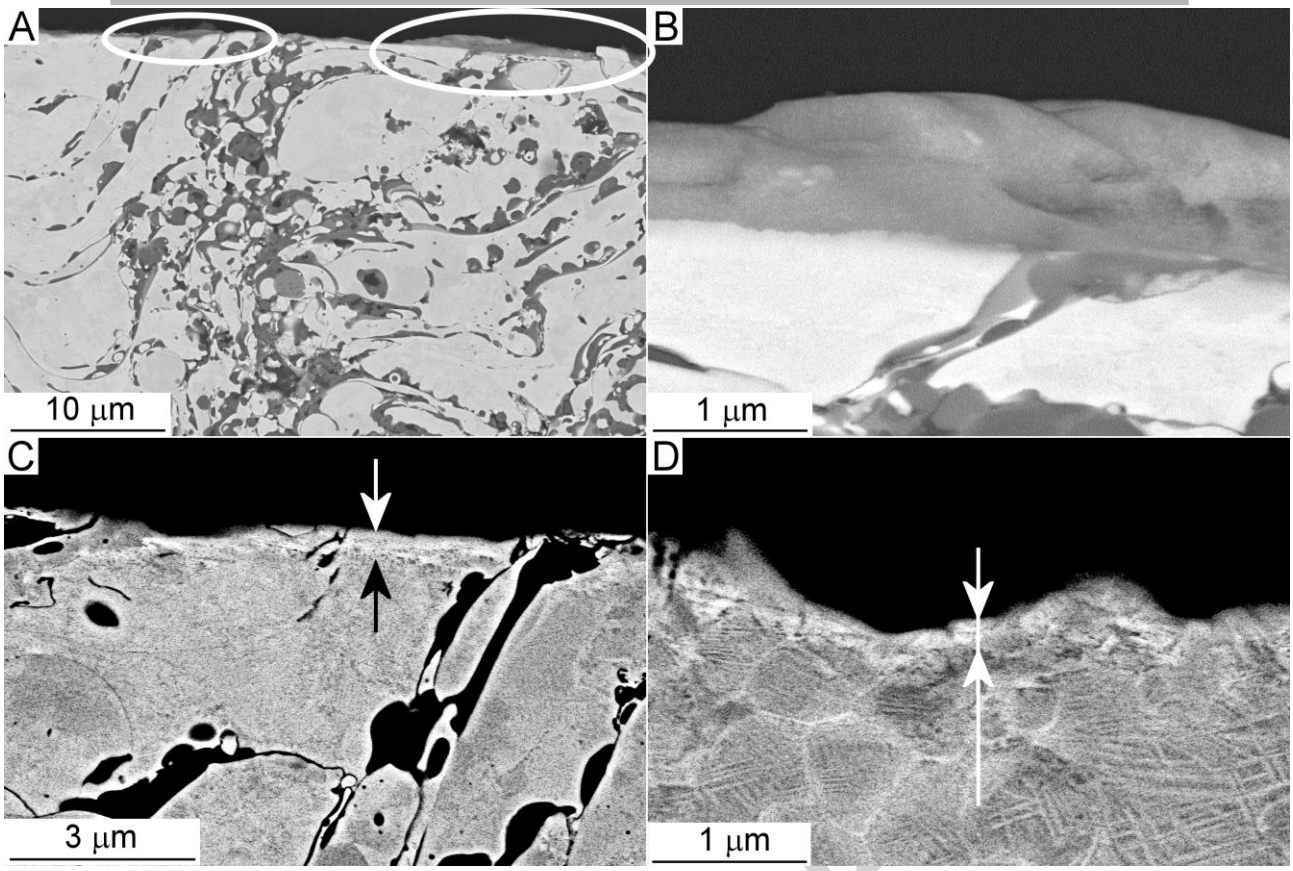

Figure 10. Cross-sectional SEM micrographs (backscattered electron images) of the wear scar produced on sample Ny10Al10BN5 after ball-on-disk testing at room temperature. A: overview (circles = debris patches); B: detail of one debris patch; C,D: detail of the sub-surface plastic deformation layer in the NiCrAlY matrix (arrows), imaged through electron channelling contrast (non-metallic inclusions and surface debris patches appear black at such contrast levels).

Accordingly, a difference also emerges between the micro-Raman spectra of oxide clusters produced on samples with different reinforcement content. With little Al_2O_3 and no *h*-BN (see the representative spectrum of sample Ny10Al10BN0 tested at room temperature in Fig. 11B), peaks at about 585 cm^{-1} and 672 cm^{-1} suggest the formation of spinels, such as $NiCr_2O_4$ [56,59,60]. A band at about 1088 cm^{-1} could additionally belong to NiO [55,56]. These phases are quite similar to those developed by in-flight oxidation of the metal alloy during plasma spraying (see Section 3.1). With higher Al_2O_3 and *h*-BN contents (see the representative spectrum of sample Ny10Al10BN5 tested at room temperature in Fig. 11B), the band at 1088 cm^{-1} disappears and a peak at ≈800 cm^{-1} is formed. These spectral features can be ascribed to a (poorly crystalline) $NiAl_2O_4$-type structure [74], suggesting tribochemical reactions between the metal debris and fragmented Al_2O_3 particles.

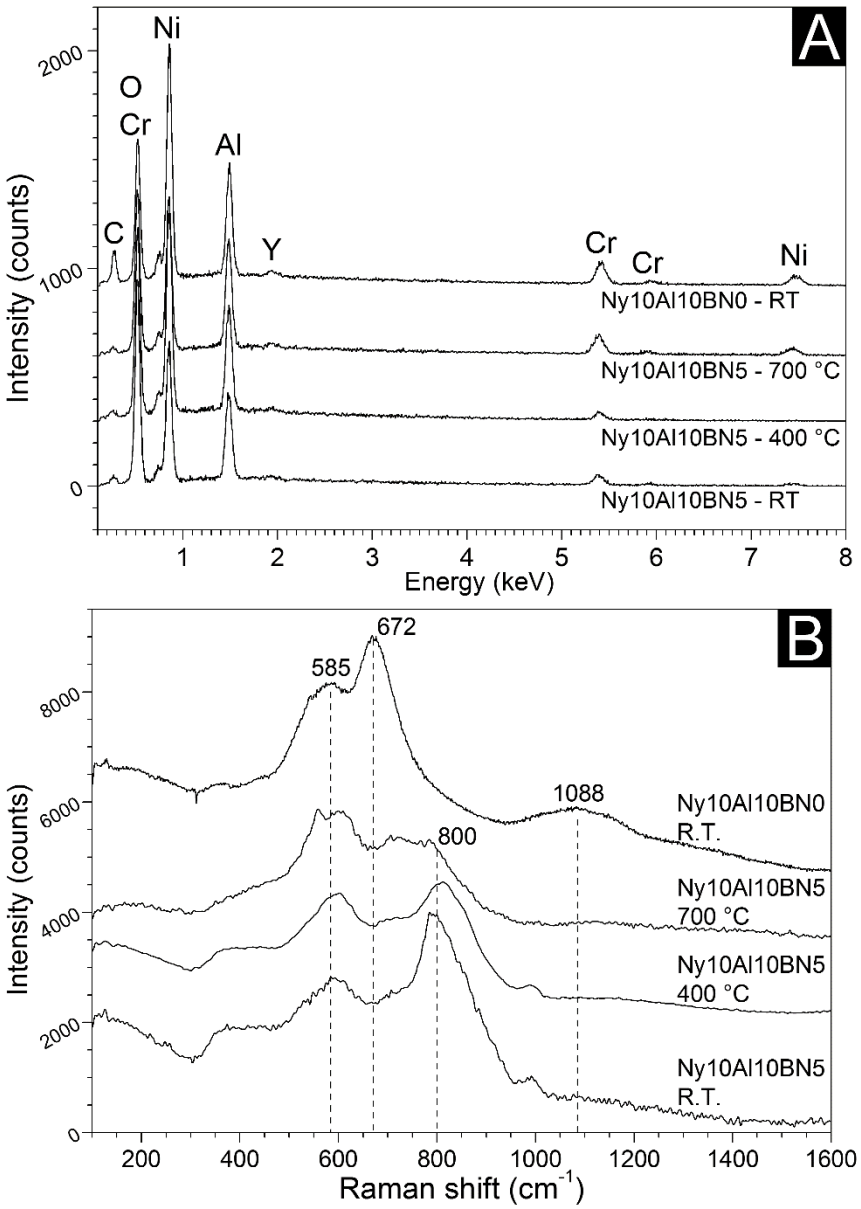

Figure 11. Representative EDX spectra of the tribofilms produced by ball-on-disk wear testing, acquired at 8 keV electron beam energy (A), and micro-Raman spectra of the same, acquired with a 532 nm-wavelength laser (B).

Moreover, the peak at 800 cm^{-1} is also characteristic of vitreous B_2O_3, consistent with the mentioned glassy halo in the electron diffraction pattern of Fig. 9D [63,64], whereas the Raman peak of *h*-BN could not be detected. It is inferred that *h*-BN particles are (at least in part) tribo-oxidised to low-melting B_2O_3, which can act as a sintering agent promoting the cohesion of the clusters. This would be consistent with the fact that the tribofilm, whilst effective in reducing wear, does not have much effect on friction (see the data in Table 4); indeed, none of the constituents

listed above ($NiAl_2O_4$-type spinels, vitreous B_2O_3) is a lamellar solid with solid lubrication capabilities.

By exploiting electron channelling contrast in backscattered electron micrographs (Fig. 10C,D), it is also noted that plastic deformation due to abrasive grooving and adhesive tearing in the NiCrAlY metal matrix is confined within a very shallow surface layer, a few hundreds of nanometres thick (see arrows in Fig. 10C,D). Below such layer, the unaltered intra-lamellar texture of the alloy is indeed recognisable (Fig. 10C,D). Adhesive tearing therefore affects the metal alloy at the intralamellar level, whereas no interlamellar cracking and delamination is seen. This behaviour differs from the interlamellar delamination observed by the authors in harder metal alloy and composite coatings [50,75], suggesting good ductility and high levels of interlamellar cohesion.

3.2.3 Sliding wear mechanisms at high temperatures

Tribo-oxidation is clearly the dominant wear mechanisms at 400 °C and 700 °C as well (Fig. 7C-F), but specific tribo-oxidation mechanisms change significantly. Instead of clusters, a more continuous "glaze" layer indeed appears at 400 °C (Fig. 7C,D) and at 700 °C (Fig. 7E,F).

Once again, the tribological role of the "glaze" layer is to avoid the abrasive and adhesive damage which the direct contact with the counterbody produces to the coating surface, as seen e.g. in the detail of an uncovered wear scar portion shown in Fig. 8C. The enhanced uniformity of the tribofilm, turning from discontinuous patches to a "glaze", is particularly effective in producing a continuous decrease of the wear rates of coatings with low Al_2O_3 and *h*-BN contents as the temperature increases up to 700 °C (Fig. 5). Better "glaze" coverage may also explain the slight decrease in friction coefficients from room temperature to 400 °C and 700 °C (Table 4).

Cross-sectional views (Fig. 12A-C) clarify that the "glaze" does not consist of compacted debris, but of oxidised NiCrAlY, through a mechanism of inward oxygen diffusion: oxidation proceeds into the metal alloy, incorporating some residual non-oxidised metal, as well as Al_2O_3 and *h*-BN

particles (Fig. 12A-C). Debris particles accumulate in areas where the layer has been delaminated during sliding (Fig. 12D).

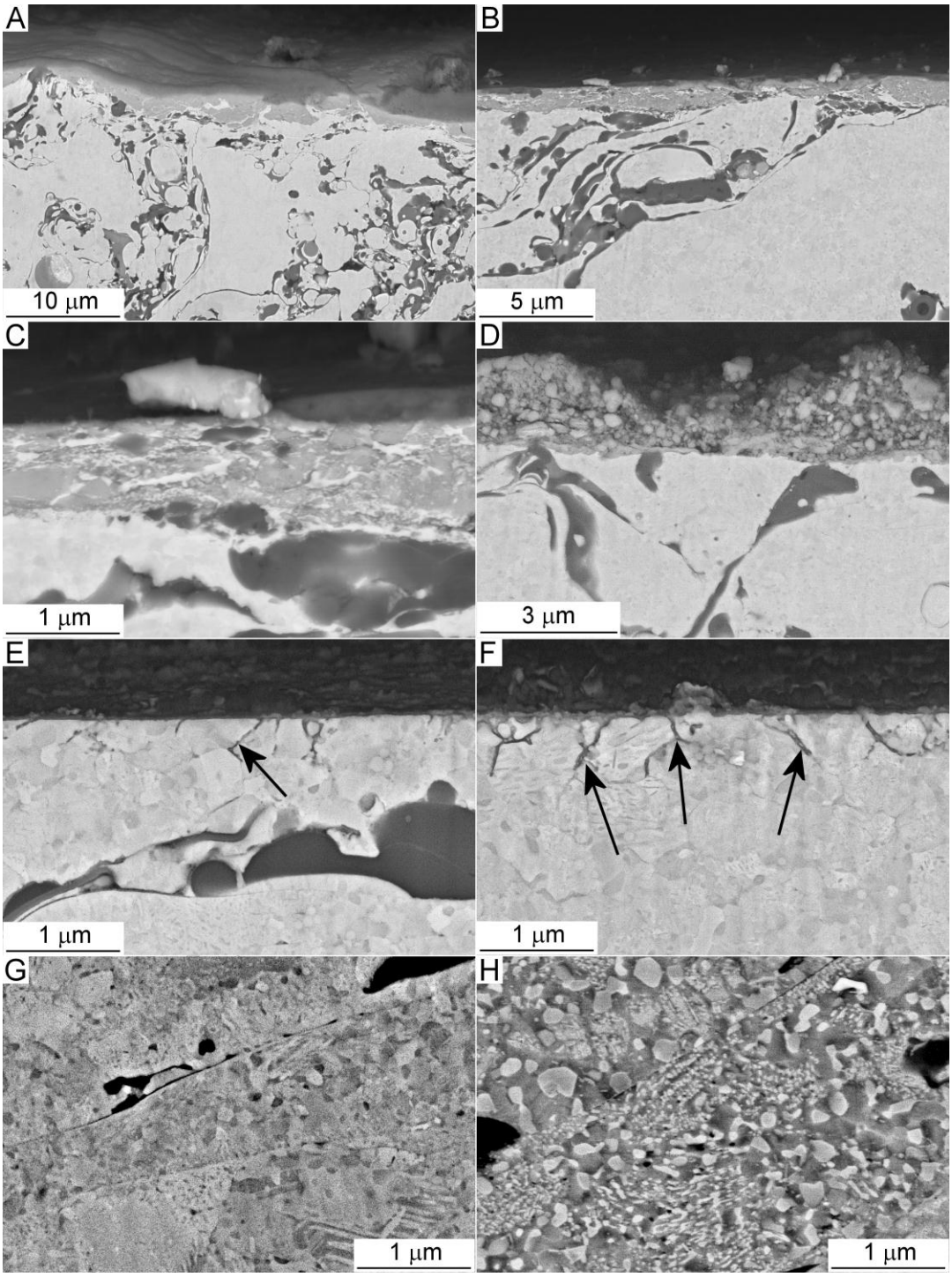

Figure 12. Cross-sectional SEM micrographs (backscattered electron images) of the wear scars of sample Ny10Al10BN5 after ball-on-disk testing at 400 °C (A) and at 700 °C (B-D); near-surface region of the same sample tested at 700 °C outside the wear scar (E,F – arrows = oxide "pegs"); cross-sectional details of the NiCrAlY matrix after holding at 700 °C: polished (G) and electrochemically etched (overpotential 2 V, time 7 s) in 0.1 M HCl (H).

The "glaze" differs from the oxide scale developed outside the wear scar. The latter is less than 100 nm thick (Fig. 12 E,F), in accordance with previous observations in [14], and its Raman spectrum (Fig. 13) is consistent with that of pure Cr_2O_3, retrieved from the RRUFF database [76] and replotted in Fig. 13 as a reference. In the authors' previous work on NiCrAlY+Al_2O_3 [14], in the absence of unambiguous experimental evidence, it had been speculated that this scale could have consisted of alumina. The new spectroscopy data presented here, obtained through an improved spectrometer version compared to that employed in the previous report, contradicts and corrects that assumption. Indeed, at 700 °C, a "relatively low" temperature if compared to service maxima of 900 – 1000 °C in the most renown application of MCrAlY-type alloys as bond coats in gas turbine blades, vanes and combustion liners [77], the formation of Cr_2O_3 instead of Al_2O_3 is consistent with the existing literature [78].

Underneath this thin (<100 nm) Cr_2O_3 scale, small oxide "pegs" propagate downwards into the metal alloy (Fig. 12E,F: see arrows). Specifically, the preferential oxidation path seems to follow the γ'-Ni_3Al matrix surrounding the re-crystallised β-NiAl phase in the microstructure of the heat-treated coating. Such re-crystallised microstructure is seen in the metal alloy by enhancing the backscatter electron contrast (Fig. 12G) and becomes even clearer after electrochemical etching (Fig. 12H), with micrometric or sub-micrometric β-NiAl protruding out of the surrounding matrix. The phase composition of the re-crystallised material is confirmed by XRD patterns (Fig. 14). β-NiAl peaks grow more intense and the (sharper) γ'-Ni_3Al peaks shift towards higher diffraction angles (= lower interplanar spacing) as the matrix releases the excess Al atoms, having higher atomic radius than Ni.

Inward diffusion of oxygen along the Al-poor γ'-Ni_3Al phase is therefore a spontaneous phenomenon affecting the NiCrAlY matrix at 700 °C. The inward diffusion process is enhanced in the wear scar, leading to more substantial oxidation of the whole alloy (instead of selective oxidation of Cr to Cr_2O_3 only) as seen from the "glaze" morphologies in Fig. 12A-C and confirmed by EDX spectra in Fig. 11A. A multiplicity of factors concur to this effect. These include flash

heating of the contact point; plastic deformation with generation of lattice defects, which probably provide additional oxygen diffusion paths; and the generation of a "tribo-plasma" in the contact area. The latter phenomenon, due to the tribo-emission of electrons from contacting surfaces in relative motion [79–81], is thought by some authors to cause the formation of extremely reactive species (ions, radicals) in the surrounding atmosphere. It has already been mentioned in [14] as a mechanism able to further enhance the tribo-chemical reaction rate.

It is important to note that *h*-BN is retained in the coating, outside the wear scar, at 400 °C and at 700 °C; indeed, its Raman peak is clearly seen when focussing the laser beam on clustered particles within the coating, outside the wear scar (Fig. 13).

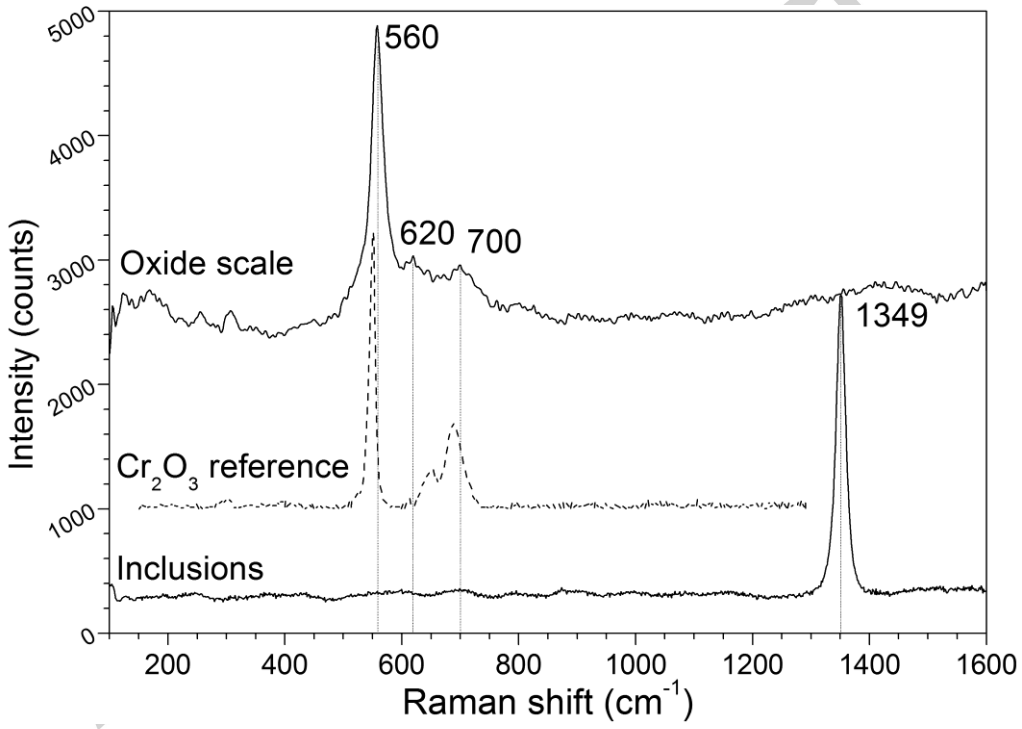

Figure 13. Representative micro-Raman spectrum of a non-metallic inclusion on sample Ny10Al10BN5 after holding at 700 °C during the wear test (outside the wear track), and spectrum of the oxide scale produced on the metal matrix (outside the wear track), compared to the reference spectrum of Cr_2O_3 taken from the RRUFF open database [76].

The Raman spectra of the "glaze" formed at 400 °C and 700 °C, on the other hand, are similar to those seen at room temperature. Namely, the spectra acquired on the wear scars of samples containing *h*-BN exhibit no sign of the latter compound (see the representative spectra acquired on

the tribofilm of sample Ny10Al10BN5 Fig. 11B). In fact, the "glaze", though able to reduce friction compared to the room-temperature condition, does not act as a solid lubricant ($\mu \approx 0.5$, Table 4). Once again, the Raman spectra suggest the presence of a $NiAl_2O_4$-type spinel with possible additions of B_2O_3 (strong peak at about 800 cm^{-1}). ICP-mass spectroscopy, with the laser ablation system focused on the "glaze" layer, confirms the presence of some B in locally variable amounts up to about 10 wt.%.

Similar to the considerations put forward in Section 3.2.2, the sintering effect of B_2O_3 probably contributed to the enhanced tribofilm stability in samples with higher Al_2O_3 and *h*-BN contents. Fig. 7A,C,E, referring to sample Ny10Al10BN0, can for instance be compared to Fig. 7B,D,F, referring to sample Ny10Al10BN5. The overall effect on wear is however much less perceivable at 400 °C and 700 °C than it was at room temperature (Table 4, Figs. 5 and 6), although, especially at 700 °C, a slight trend of decreasing wear rates with increasing amounts of Al_2O_3 and *h*-BN can be seen in Fig. 5C. Even when the coatings contain little or no *h*-BN and Al_2O_3, indeed, enough "glaze" is formed by tribo-oxidation of NiCrAlY alone to mediate most of the contact with the counterbody. Taking samples Ny10Al10BN0 and Ny10Al10BN5 (shown in Fig. 7) as an example, the change in wear scar morphology from Fig. 7A (sample Ny10Al10BN0, room temperature) to Figs. 7C,E (sample Ny10Al10BN0, high temperatures) is much more remarkable than is the difference between the morphologies in Fig. 7C,E and in Fig. 7D,F (sample Ny10Al10BN5, high temperature).

The analysis has therefore revealed that *h*-BN did not perform a solid lubricant action, contrary to the initial expectations put forward in the Introduction. Regardless of the composition, the friction coefficient values listed in Table 4 are indeed >0.65 at room temperature and lay around 0.5 at higher temperatures. The addition of *h*-BN was instead found to be beneficial for wear resistance. It favoured the onset of a more stable tribo-oxidational wear regime at all test temperatures, through a mechanism that probably involves tribo-oxidation of *h*-BN to B_2O_3, acting as a sintering agent to

improve the strength and cohesion of the different types of tribofilm developed at room and at high temperatures.

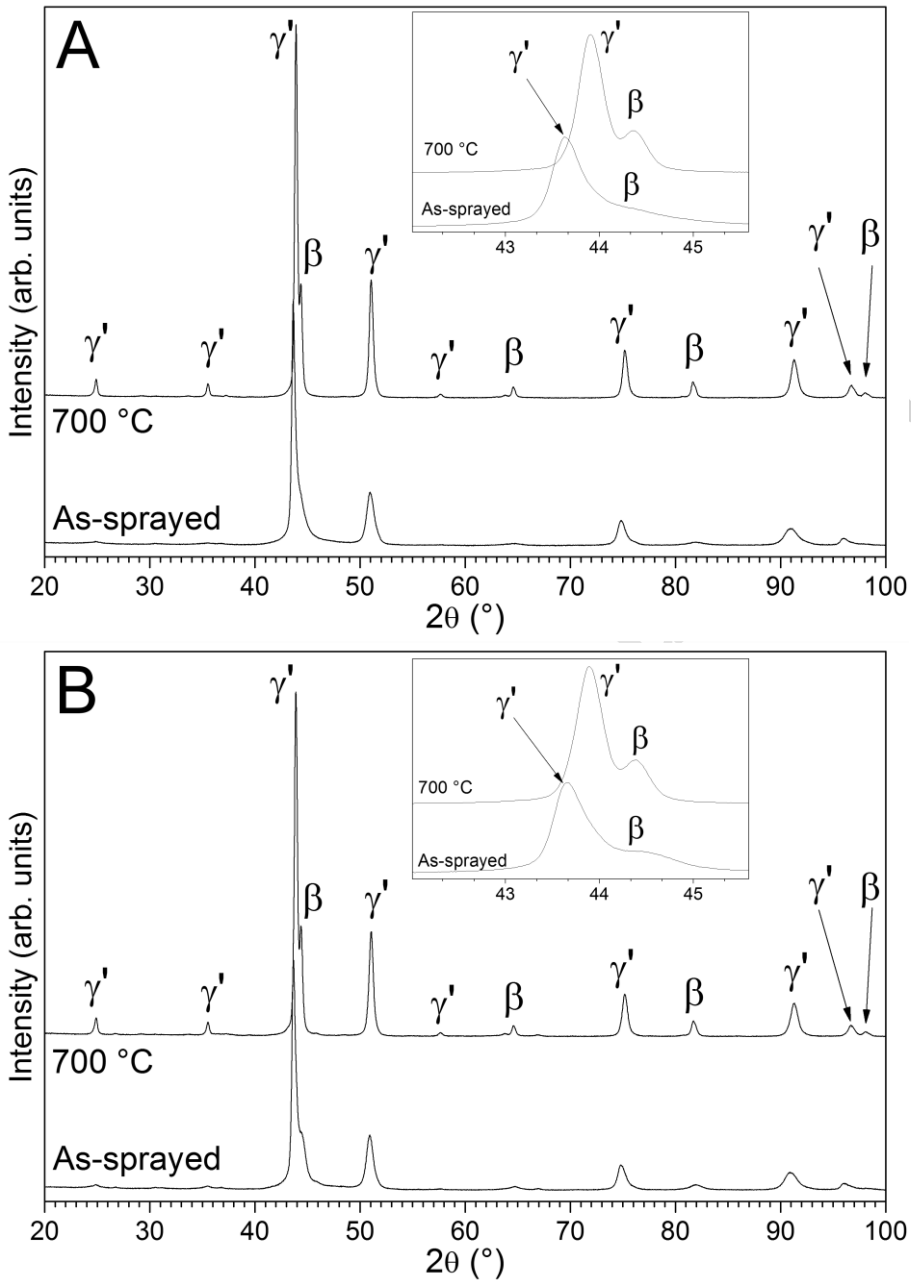

Figure 14. Comparison between the XRD patterns of samples Ny10Al10BN0 (A) and Ny10Al10BN5 (B) in as-sprayed condition and after heating at 700 °C during the ball-on-disk test. The inset shows a detail of the area around 2θ = 44°. Legend: γ' = γ'-Ni_3Al (JCPDF 3-65-140); β = β-NiAl (JCPDF 3-65-431). The peak of γ-Al_2O_3, indicated in Fig. 3, is not labelled in this figure.

Conclusions

Using a novel atmospheric plasma spray process with simultaneous, "hybrid" injection of dry and liquid feedstock, composite coatings consisting of a NiCrAlY metal matrix containing from ≈1 to 10 wt.% Al_2O_3 and 0 to ≈9 wt.% *h*-BN sub-micrometric particles were produced. The presence of undecomposed *h*-BN is confirmed by micro-Raman spectra.

The Al_2O_3 and *h*-BN sub-micrometric particles tend to cluster in the coatings, attaching preferentially to prominent asperities, and a clear co-deposition effect is noted. Even with a constant feed rate of Al_2O_3 suspension, the amount of Al_2O_3 in the coatings increases when *h*-BN is also introduced into the plasma jet.

Although Al_2O_3 and *h*-BN particles do not alter the hardness and the elastic modulus of the coatings, they enhance the sliding wear resistance. The effect is especially marked at room temperature, as Al_2O_3 and *h*-BN favour the formation of protective, oxide-based tribofilms consisting of patches of smeared debris particles. In particular, *h*-BN is tribo-oxidised to B_2O_3, probably acting as a "sintering agent" (due to its low melting point) to enhance the mechanical strength of the tribofilm.

The effect of Al_2O_3 and *h*-BN is less marked at 400 °C and at 700 °C, since the high-temperature tribofilms mostly consist of a dense "glaze" formed by tribochemically-accelerated oxidation of the NiCrAlY alloy. Al_2O_3 and *h*-BN particles in the tribofilm enhance the stability of the "glaze".

As a result, samples containing at least 5 wt.% each of Al_2O_3 and *h*-BN are potentially suitable for a variety of industrial applications involving operation of a wide temperature range, since they exhibit quite stable sliding wear rates around 10^{-5} $mm^3/(Nm)$ from room temperature to 700 °C.

It is further concluded that *h*-BN does not exert a solid lubricant action: by contrast, it enhances the tribofilm stability through a tribo-oxidation mechanism, helping to reduce the wear rates.

Acknowledgements

The authors would like to acknowledge the support of the University of Modena and Reggio Emilia through the FAR ("Fondo di Ateneo per la Ricerca") funding scheme for the project entitled "Meccanismi di attrito e usura di superfici autolubrificanti alla multiscale (Friction and wear mechanisms of multiscale self-lubricating surfaces)".

References

[1] A. Killinger, R. Gadow, G. Mauer, A. Guignard, R. Vaßen, D. Stöver, Review of new developments in suspension and solution precursor thermal spray processes, J. Therm. Spray Technol. 20 (2011) 677–695.

[2] P. Fauchais, G. Montavon, R.S. Lima, B.R. Marple, Engineering a new class of thermal spray nano-based microstructures from agglomerated nanostructured particles, suspensions and solutions: an invited review, J. Phys. D. Appl. Phys. 44 (2011) 093001.

[3] P. Fauchais, R. Etchart-Salas, V. Rat, J.F. Coudert, N. Caron, K. Wittmann-Ténèze, Parameters Controlling Liquid Plasma Spraying: Solutions, Sols, or Suspensions, J. Therm. Spray Technol. 17 (2008) 31–59.

[4] F.L. Toma, A. Potthoff, L.M. Berger, C. Leyens, Demands, Potentials, and Economic Aspects of Thermal Spraying with Suspensions: A Critical Review, J. Therm. Spray Technol. 24 (2015) 1143–1152.

[5] E.M. Cotler, D. Chen, R.J. Molz, Pressure-based liquid feed system for suspension plasma spray coatings, J. Therm. Spray Technol. 20 (2011) 967–973.

[6] O. Tingaud, A. Bacciochini, G. Montavon, A. Denoirjean, P. Fauchais, Suspension DC plasma spraying of thick finely-structured ceramic coatings: Process manufacturing mechanisms, Surf. Coat. Technol. 203 (2009) 2157–2161.

[7] J. Karthikeyan, C. Berndt, Nanomaterial deposits formed by DC plasma spraying of liquid feedstocks, J. Am. Ceram. Soc. 28 (1998) 121–128.

[8] R. Ahmed, O. Ali, N.H. Faisal, N.M. Al-Anazi, S. Al-Mutairi, F.L. Toma, et al., Sliding wear investigation of suspension sprayed WC-Co nanocomposite coatings, Wear 322-323 (2015) 133–150.

[9] F. Cipri, F. Marra, G. Pulci, J. Tirillò, C. Bartuli, T. Valente, et al., Plasma sprayed composite coatings obtained by liquid injection of secondary phases, Surf. Coat. Technol. 203 (2009) 2116–2124.

[10] S.V. Joshi, G. Sivakumar, T. Raghuveer, R.O. Dusane, Hybrid Plasma-Sprayed Thermal Barrier Coatings Using Powder and Solution Precursor Feedstock, J. Therm. Spray Technol. 23 (2014) 616–624.

[11] A. Lohia, G. Sivakumar, M. Ramakrishna, S.V. Joshi, Deposition of Nanocomposite Coatings Employing a Hybrid APS + SPPS Technique, J. Therm. Spray Technol. 23 (2014) 1054–1064.

[12] G. Sivakumar, S. V. Joshi, Composite Coatings Employing a Novel Hybrid Powder and Solution-Based Plasma Spray Technique for Tribological Applications, in: M. Roy, J.P. Davim (Eds.), Therm. Sprayed Coatings Their Tribol. Performances, IGI Global, Hershey, PA, USA, 2015: pp. 61–87.

[13] S. V. Joshi, G. Sivakumar, Hybrid Processing with Powders and Solutions: A Novel Approach to Deposit Composite Coatings, J. Therm. Spray Technol. 24 (2015) 1166–1186.

[14] G. Bolelli, A. Candeli, L. Lusvarghi, A. Ravaux, K. Cazes, A. Denoirjean, et al., Tribology

of NiCrAlY+Al_2O_3 composite coatings by plasma spraying with hybrid feeding of dry powder+suspension, Wear 344-345 (2015) 69–85.

[15] J. Voyer, B.R. Marple, Tribological performance of thermally sprayed cermet coatings containing solid lubricants, Surf. Coat. Technol. 127 (2000) 155–166.

[16] Y. Tsunekawa, I. Ozdemir, M. Okumiya, Plasma Sprayed Cast Iron Coatings Containing Solid Lubricant Graphite and h-BN Structure, J. Therm. Spray Technol. 15 (2006) 239–245.

[17] W. Zórawski, R. Chatys, N. Radek, J. Borowiecka-Jamrozek, Plasma-sprayed composite coatings with reduced friction coefficient, Surf. Coat. Technol. 202 (2008) 4578–4582.

[18] J. Yuan, Y. Zhu, X. Zheng, H. Ji, T. Yang, Fabrication and evaluation of atmospheric plasma spraying WC–Co–Cu–MoS_2 composite coatings, J. Alloys Compd. 509 (2011) 2576–2581.

[19] L. Du, C. Huang, W. Zhang, T. Li, W. Liu, Preparation and wear performance of NiCr/Cr_3C_2-NiCr/hBN plasma sprayed composite coating, Surf. Coat. Technol. 205 (2011) 3722–3728.

[20] N. Espallargas, S. Armada, A New Type of Self-lubricated Thermal Spray Coatings: Liquid Lubricants Embedded in a Metal Matrix, J. Therm. Spray Technol. 24 (2015) 222–234.

[21] S. Armada, R. Schmid, S. Equey, I. Fagoaga, N. Espallargas, Liquid-solid self-lubricated coatings, J. Therm. Spray Technol. 22 (2013) 10–17.

[22] N. Espallargas, L. Vitoux, S. Armada, The wear and lubrication performance of liquid-solid self-lubricated coatings, Surf. Coat. Technol. 235 (2013) 342–353.

[23] G. Mariani, Selection and Application of Solid Lubricants as Friction Modifiers, in: L.R. Rudnick (Ed.), Lubr. Addit. Chem. Appl., CRC Press, Boca Raton, FL, USA, 2009.

[24] R.W. Bruce, Solid Lubricants, in: R.W. Bruce (Ed.), Handb. Lubr. Tribol. Vol. II Theory Des., Second Edi, CRC Press, Boca Raton, FL, USA, 2015.

[25] N. Kostoglou, K. Polychronopoulou, C. Rebholz, Thermal and chemical stability of hexagonal boron nitride (h-BN) nanoplatelets, Vacuum 112 (2015) 42–45.

[26] C. DellaCorte, B. Edmonds, NASA PS400: a new high temperature solid lubricant coating for high temperature wear applications, Cleveland, OH, USA, 2009.

[27] H.E. Sliney, Wide temperature spectrum self-lubricating coatings prepared by plasma spraying, Thin Solid Films 64 (1979) 211–217.

[28] G. Kim, H. Choi, C. Han, S. Uhm, C. Lee, Characterization of atmospheric plasma spray NiCr-Cr_2O_3-Ag-CaF_2/BaF_2 coatings, Surf. Coat. Technol. 195 (2005) 107–115.

[29] W. Wang, Application of a high temperature self-lubricating composite coating on steam turbine components, Surf. Coat. Technol. 177-178 (2004) 12–17.

[30] C.B. Huang, L.Z. Du, W.G. Zhang, Microstructure, mechanical and tribological characteristics of plasma, detonation gun and HVOF sprayed NiCr/Cr_3C_2–BaF_2.CaF_2 coatings, Surf. Eng. 27 (2011) 762–769.

[31] C.E. Fanning, T.A. Blanchet, High-temperature evaluation of solid lubricant coatings in a foil thrust bearing, Wear 265 (2008) 1076–1086.

[32] A. Joulia, G. Bolelli, E. Gualtieri, L. Lusvarghi, S. Valeri, M. Vardelle, et al., Comparing the deposition mechanisms in suspension plasma spray (SPS) and solution precursor plasma spray (SPPS) deposition of yttria-stabilised zirconia (YSZ), J. Eur. Ceram. Soc. 34 (2014) 3925–3940.

[33] G. Mauer, A. Guignard, R. Vaßen, D. Stöver, Process diagnostics in suspension plasma spraying, Surf. Coat. Technol. 205 (2010) 961–966.

[34] R. Vaßen, H. Kaßner, G. Mauer, D. Stöver, R. Vaen, H. Kaner, et al., Suspension plasma spraying: Process characteristics and applications, J. Therm. Spray Technol. 19 (2010) 219–225.

[35] G. Mauer, R. Vaßen, D. Stöver, Preliminary study on the TriplexPro^{TM}-200 gun for atmospheric plasma spraying of yttria-stabilized zirconia, Surf. Coat. Technol. 202 (2008) 4374–4381.

[36] J.F. Coudert, V. Rat, The role of torch instabilities in the suspension plasma spraying process, Surf. Coat. Technol. 205 (2010) 949–953.

[37] H. Zimmermann, H.-M. Höhle, Triplex II – Die Entwicklung eines wirtschaftlichen Hochleistungsplasmaspritzsystems für höchste Qualitätsansprüche selbst unter extremen Produktionsbedingungen, in: F.-W. Bach, K. Möhwald, A. Laarmann, T. Wenz (Eds.), Mod. Beschichtungsverfahren, WILEY-VCH Verlag GmbH & Co., Weinheim, Germany, 2005: pp. 177–198.

[38] ISO 14577-1:2002 - Metallic materials — Instrumented indentation test for hardness and materials parameters — Part 1: Test method, International Organization for Standardization (ISO), Geneva, Switzerland, 2002.

[39] ISO 14577-4:2007 - Metallic materials — Instrumented indentation test for hardness and materials parameters — Part 4: Test method for metallic and non-metallic coatings, International Organization for Standardization (ISO), Geneva, Switzerland, 2007.

[40] ISO 14577-2:2002 - Metallic materials — Instrumented indentation test for hardness and materials parameters — Part 2: Verification and calibration of testing machines, International Organization for Standardization (ISO), Geneva, Switzerland, 2002.

[41] B. Bhushan, Principles and Applications of Tribology, Second Edi, John Wiley & Sons Ltd., Chichester, UK, 2013.

[42] S.M. Hsu, M.C. Shen, Wear Maps, in: B. Bhushan (Ed.), Mod. Tribol. Handb. – Vol. 1, CRC Press, Boca Raton, FL, USA, 2001: pp. 317–359.

[43] W. Tillmann, L. Hagen, D. Stangier, I.A. Laemmerhirt, D. Biermann, P. Kersting, et al., Wear behavior of bio-inspired and technologically structured HVOF sprayed NiCrBSiFe coatings, Surf. Coat. Technol. 280 (2015) 16–26.

[44] J.A. Picas, M. Punset, M. Teresa Baile, E. Martín, A. Forn, Tribological evaluation of HVOF thermal-spray coatings as a hard chrome replacement, Surf. Interface Anal. 43 (2011) 1346–1353.

[45] J.A. Picas, Y. Xiong, M. Punset, L. Ajdelsztajn, A. Forn, J.M. Schoenung, Microstructure and wear resistance of WC-Co by three consolidation processing techniques, Int. J. Refract. Met. Hard Mater. 27 (2009) 344–349.

[46] J.M. Guilemany, N. Espallargas, J. Fernández, P.H. Suegama, A.V. Benedetti, High-velocity oxyfuel Cr_3C_2-NiCr replacing hard chromium coatings, J. Therm. Spray Technol. 14 (2005) 335–341.

[47] L.M. Berger, M. Woydt, S. Saaro, Comparison of self-mated hardmetal coatings under dry sliding conditions up to 600 °C, Wear 266 (2009) 406–416.

[48] Š. Houdková, E. Smazalová, M. Vostřák, J. Schubert, Properties of NiCrBSi coating, as sprayed and remelted by different technologies, Surf. Coat. Technol. 253 (2014) 14–26.

[49] J.M. Guilemany, N. Cinca, J. Fernández, S. Sampath, Erosion, abrasive, and friction wear behavior of iron aluminide coatings sprayed by HVOF, J. Therm. Spray Technol. 17 (2008) 762–773.

[50] G. Bolelli, B. Bonferroni, J. Laurila, L. Lusvarghi, A. Milanti, K. Niemi, et al., Micromechanical properties and sliding wear behaviour of HVOF-sprayed Fe-based alloy coatings, Wear 276-277 (2012) 29–47.

[51] D.E. Crawmer, Coating Structures, Properties, and Materials, in: R.C. Tucker Jr. (Ed.), ASM Handb. - Vol. 5A Therm. Spray Technol., ASM International, Materials Park, OH, USA, OH, USA, 2013: pp. 60–64.

[52] A. Valarezo, S. Sampath, An integrated assessment of process-microstructure-property relationships for thermal-sprayed NiCr coatings, J. Therm. Spray Technol. 20 (2011) 1244–1258.

[53] R. McPherson, Formation of metastable phases in flame- and plasma-prepared alumina, J. Mater. Sci. 8 (1973) 851–858.

[54] K. VanEvery, M.J.M. Krane, R.W. Trice, H. Wang, W. Porter, M. Besser, et al., Column Formation in Suspension Plasma-Sprayed Coatings and Resultant Thermal Properties, J. Therm. Spray Technol. 20 (2011) 817–828.

[55] L.J. Oblonsky, T.M. Devine, A surface enhanced Raman spectroscopic study of the passive films formed in borate buffer on iron, nickel, chromium and stainless steel, Corros. Sci. 37 (1995) 17–41.

[56] J.H. Kim, I.S. Hwang, Development of an in situ Raman spectroscopic system for surface oxide films on metals and alloys in high temperature water, Nucl. Eng. Des. 235 (2005) 1029–1040.

[57] S.-H. Shim, T.S. Duffy, R. Jeanloz, C.-S. Yoo, V. Iota, Raman spectroscopy and x-ray diffraction of phase transitions in Cr_2O_3 to 61 GPa, Phys. Rev. B 69 (2004) 144107.

[58] J.E. Maslar, W.S. Hurst, W.J. Bowers, J.H. Hendricks, M.I. Aquino, I. Levin, In situ Raman spectroscopic investigation of chromium surfaces under hydrothermal conditions, Appl. Surf. Sci. 180 (2001) 102–118.

[59] M. Da Cunha Belo, M. Walls, N.E. Hakiki, J. Corset, E. Picquenard, G. Sagon, et al.,

Composition, structure and properties of the oxide films formed on the stainless steel 316L in a primary type PWR environment, Corros. Sci. 40 (1998) 447–463.

[60] H.D. Lutz, B. Müller, H.J. Steiner, Lattice vibration spectra. LIX. Single crystal infrared and Raman studies of spinel type oxides, J. Solid State Chem. 90 (1991) 54–60.

[61] S. Reich, A. Ferrari, R. Arenal, A. Loiseau, I. Bello, J. Robertson, Resonant Raman scattering in cubic and hexagonal boron nitride, Phys. Rev. B 71 (2005) 1–12.

[62] N.R. Arutyunyan, E.D. Obraztsova, M. Silly, P. Jaffrennou, B. Attal-Tretout, A. Loiseau, et al., Thermal effects in Raman spectra of hexagonal boron nitride and nanotube-containing boron nitride soot, Phys. Status Solidi Basic Res. 243 (2006) 3316–3319.

[63] J.H. Hibben, The Constitution of some Boric Oxide Compounds, Am. J. Sci. 35-A (1938) 113–125.

[64] G.E. Walrafen, S.R. Samanta, P.N. Krishnan, Raman investigation of vitreous and molten boric oxide, J. Chem. Phys. 72 (1980) 113–120.

[65] G. Busca, Structural, Surface, and Catalytic Properties of Aluminas, in: F.C. Jentoft (Ed.), Adv. Catal. - Vol. 57, Elsevier Academic Press, London, UK, 2014: pp. 319–404.

[66] Q. Ma, D.R. Clarke, Piezospectroscopic Determination of Residual-Strsses in Polycrystalline Alumina, J. Am. Ceram. Soc. 77 (1994) 298–302.

[67] R.J. Christensen, D.M. Lipkin, D.R. Clarke, K. Murphy, Nondestructive evaluation of the oxidation stresses through thermal barrier coatings using Cr^{3+} piezospectroscopy, Appl. Phys. Lett. 69 (1996) 3754.

[68] C. Delbos, J. Fazilleau, V. Rat, J.F. Coudert, P. Fauchais, B. Pateyron, Phenomena involved in suspension plasma spraying part 2: Zirconia particle treatment and coating formation, Plasma Chem. Plasma Process. 26 (2006) 393–414.

[69] G. Bolelli, N. Stiegler, D. Bellucci, V. Cannillo, R. Gadow, A. Killinger, et al., Deposition mechanisms in high velocity suspension spraying: Case study for two bioactive materials, Surf. Coat. Technol. 210 (2012) 28–45.

[70] K. Kato, K. Adachi, Wear Mechanisms, in: B. Bhushan (Ed.), Mod. Tribol. Handb. – Vol. 1, CRC Press, Boca Raton, FL, USA, 2001: pp. 273–300.

[71] K. Komvopoulos, Adhesive Wear, in: R.W. Bruce (Ed.), Handb. Lubr. Tribol. Vol. II Theory Des., Second Edi, CRC Press, Boca Raton, FL, USA, 2012.

[72] G. Straffelini, Friction and Wear: Methodologies for Design and Control, Springer International Publishing AG, Cham, Switzerland, 2015.

[73] D.A. Rigney, Sliding Wear of Metals, Annu. Rev. Mater. Sci. 18 (1988) 141–163.

[74] M.A. Laguna-Bercero, M.L. Sanjuán, R.I. Merino, Raman spectroscopic study of cation disorder in poly- and single crystals of the nickel aluminate spinel, J. Phys. Condens. Matter 19 (2007) 186217.

[75] G. Bolelli, T. Börner, A. Milanti, L. Lusvarghi, J. Laurila, H. Koivuluoto, et al., Tribological

behavior of HVOF- and HVAF-sprayed composite coatings based on Fe-Alloy+WC–12% Co, Surf. Coat. Technol. 248 (2014) 104–112.

[76] B. Lafuente, R.T. Downs, H. Yang, N. Stone, The power of databases: the RRUFF project, in: T. Armbruster, R.M. Danisi (Eds.), Highlights Mineral. Crystallogr., De Gruyter, Berlin, Germany, 2015: pp. 1–30.

[77] S. Bose, High Temperature Coatings, Butterworth-Heinemann, Oxford, UK, 2007.

[78] J.R. Nicholls, N.J. Simms, W.Y. Chan, H.E. Evans, Smart overlay coatings - Concept and practice, Surf. Coat. Technol. 149 (2002) 236–244.

[79] C.K. Kajdas, Importance of the triboemission process for tribochemical reaction, Tribol. Int. 38 (2005) 337–353.

[80] G.J. Molina, M.J. Furey, A.L. Ritter, C. Kajdas, Triboemission from alumina, single crystal sapphire, and aluminum, Wear 249 (2001) 214–219.

[81] K. Nakayama, Chemi-emission of electrons from metal surfaces in the cutting process due to metal/gas interactions, Tribol. Int. 28 (1995) 507–515.

Highlights

- Composite coatings consist of a NiCrAlY matrix containing Al_2O_3 and *h*-BN particles
- Dry powder and liquid feedstock were co-injected in a “hybrid” plasma spray process
- Al_2O_3 and *h*-BN enhance sliding wear resistance by promoting stable oxide tribofilms
- *h*-BN, tribo-oxidised to B_2O_3, acts as sintering agent to enhance tribofilm stability
- With ≥5wt.% Al_2O_3 and *h*-BN, coating wear rates are ≈10^{-5} $mm^3/(Nm)$ from R.T. to 700 °C